JOURNAL OF GEOPHYSICAL RESEARCH: OCEANS, VOL. 119, 1–17, doi:10.1002/2013JC009466, 2014

Effects of waves on coastal water dispersion in a small estuarine bay

M. T. Delpey,[1] F. Ardhuin,[2] P. Otheguy,[1] and A. Jouon[1]

Received 27 September 2013; revised 2 December 2013; accepted 9 December 2013.

[1] A three-dimensional wave-current model is used to investigate wave-induced circulations in a small estuarine bay and its impact on freshwater exchanges with the inner shelf, related to stratified river plume dispersion. Modeled salinity fields exhibit a lower salinity surface layer due to river outflows, with typical depth of 1 m inside the bay. The asymmetric wave forcing on the bay circulation, related to the local bathymetry, significantly impacts the river plumes. It is found that the transport initiated in the surf zone by the longshore current can oppose and thus reduce the primary outflow of freshwater through the bay inlets. Using the model to examine a high river runoff event occurring during a high-energy wave episode, waves are found to induce a 24 h delay in freshwater evacuation. At the end of the runoff event, waves have reduced the freshwater flux to the ocean by a factor 5, and the total freshwater volume inside the bay is increased by 40%. According to the model, and for this event, the effect of the surf zone current on the bay flushing is larger than that of the wind. The freshwater balance is sensitive to incident wave conditions. Maximum freshwater retention is found for intermediate offshore wave heights $1\ \mathrm{m} < H_s < 2\ \mathrm{m}$. For higher-energy waves, the increase in the longshore current reduces the retention, which is two times lower for $H_s = 4$ m than for $H_s = 2$ m.

Citation: Delpey, M. T., F. Ardhuin, P. Otheguy, and A. Jouon (2014), Effects of waves on coastal water dispersion in a small estuarine bay, *J. Geophys. Res. Oceans*, *119*, doi:10.1002/2013JC009466.

1. Introduction

[2] Coastal waters are the receptacle for pollutants from estuarine watersheds, especially fecal indicator bacteria [*Boehm et al*., 2002; *Reeves et al*., 2004]. The related degradation of the water quality increases human health risks and leads to large economic impacts [*Grant et al*., 2005; *Given et al*., 2006]. Terrestrial storm water runoff often drains first onto rivers and tidal channels, finding its way into the coastal zone with freshwater inflows. In that case, nearshore concentrations of fecal indicator bacteria are closely related to river plumes dispersion and freshwater exchanges with the inner shelf [e.g., *Ahn et al*., 2005]. Estuarine bays and lagoons are particularly impacted by such contaminations, as freshwater concentrates in these coastal systems due to their partial separation from the ocean [e.g., *Fiandrino et al*., 2003; *Pereira et al*., 2009]. Depending on the system morphology and the local wave climate, ocean waves may strongly impact dispersion processes. Surf zone transport and mixing affect the suspended matter alongshore distribution and nearshore retention [*Boehm et al*., 2005; *Feddersen*, 2007; *Spydell et al*., 2007, 2009; *Reniers et al*., 2009]. Waves also affect exchanges between the nearshore and the inner shelf [*Lentz et al*., 2008].

[3] The interaction of ocean waves and nearshore currents can be decomposed in several processes. The momentum carried by waves across the ocean is released in the surf zone and captured in intense currents and sea level changes. Waves contribute to vertical mixing in deep or shallow water as turbulent kinetic energy is enhanced at the surface by wave breaking [*Craig and Banner*, 1994; *Terray et al*., 1996; *Feddersen*, 2012a, 2012b]. The mean wave momentum, or Stokes drift [*Stokes*, 1847], contributes to the advection as a surface-intensified current which adds to the mean current. Following the pioneering work of *Longuet-Higgins and Stewart* [1962, 1964], modeling of surf zone circulations has long been based on phase-averaged and depth-averaged equations, notably due to their computational efficiency. However, it appeared that the vertical shear of the mean flow can influence lateral mixing [*Svendsen and Putrevu*, 1994]. Moreover, in a vertically sheared flow, depth-integrated velocities are not representative of velocities advecting a tracer with nonuniform vertical distribution. In fact, the Stokes drift always exhibits a strong vertical shear near the surface [*Miche*, 1944; *Ardhuin et al*., 2008b]. In the nearshore, this leads to large vertical variations of the total cross-shore current. Also, laboratory and field observations suggested that rip currents might vary from depth-uniform to depth-varying outside the breakers, with higher velocities near the surface [e.g., *Haas and Svendsen*, 2002; *Reniers et al*., 2009]. To capture the transport of a tracer in the presence of waves, the vertical structure of the flow may thus be needed.

[1]Centre Rivages Pro Tech, Lyonnaise des Eaux, Bidart, France.
[2]Laboratoire d'Océanographie Spatiale, IFREMER, Plouzané, France.

Corresponding author: M. T. Delpey, Centre Rivages Pro Tech, Lyonnaise des Eaux, Technopole Izarbel, 2, allée Théodore Monod, FR-64210 Bidart, France. (matthias.delpey@ponts.org)

2169-9275/14/10.1002/2013JC009466

[4] During the last decade, wave-current three-dimensional (3-D) approaches have been proposed to account for the vertical shear of wave momentum and forcing [e.g., *Groeneweg*, 1999; *Mellor*, 2003; *Mc Williams et al*., 2004; *Ardhuin et al*., 2008b; *Aiki and Greatbatch*, 2012]. Some of these have been further adapted into existing ocean numerical models and applied to reproduce observed circulations [e.g., *Uchiyama et al*., 2009] and nearshore dispersion [e.g., *Reniers et al*., 2009]. The main distinctions between the different formulations are (1) the use of an Eulerian or Lagrangian point of view and (2) the separation or not of the momentum into wave and mean flow contributions [*Lane et al*., 2007; *Bennis et al*., 2011]. For the first aspect, truly Eulerian approach requires a mathematical extrapolation of the velocity profile from the trough level to the mean sea level in order to define the mean flow in the crest-to-trough region [*Mc Williams et al*., 2004]. This can be avoided in the Lagrangian framework, as the particle-following average is well defined in the whole water column [*Andrews and McIntyre*, 1978]. The second difference is the distinction of wave and current momentum first introduced in depth-averaged equations by *Garrett* [1976]. This distinction has the main benefit of avoiding a common turbulent parameterization for both waves and current, as the Stokes drift is not mixed by turbulence unlike the mean current. It also turns out that the equation for the mean flow momentum only requires wave-induced forcing terms obtained from traditional two-dimensional wave models, whereas forcing for the full momentum requires more complex wave models, accurate to first order in parameters like the bottom slope [*Ardhuin et al*., 2008a]. Taking advantages of both Lagrangian framework and momentum separation, *Ardhuin et al*. [2008b] (hereinafter A08) proposed a 3-D wave-current approach based on the *Generalized Lagrangian Mean* (GLM) theory introduced by *Andrews and McIntyre* [1978]. An asymptotic formulation of the exact GLM-equations is provided to the second order in wave nonlinearities. The obtained set of equations is nondivergent, thanks to a transformation of the vertical coordinate. The A08 formulation is consistent with *Mc Williams et al*. [2004] to the considered order of approximation in the limit of a weak mean-current vertical shear [*Ardhuin et al*., 2008b]. *Bennis et al*. [2011] confirmed the ability of A08 formulation to provide the vertical structure of the flow by numerical modeling of an adiabatic configuration. *Michaud et al*. [2012] further showed the consistency of the solution obtained from A08 formulation with results from *Haas and Warner* [2009] and *Uchiyama et al*. [2010] in the case of obliquely incident waves breaking on a plane beach. Model results were further applied to a realistic configuration on the French Mediterranean coast.

[5] Following these works, the A08 formulation shall be used in the present study. The corresponding set of equations was implemented in the 3-D primitive equations model MOHID Water [*Martins et al*., 2001; *Braunschweig et al*., 2004]. This model is used to investigate dispersion and mixing mechanisms in the bay of Saint Jean de Luz-Ciboure under the combined influence of winds, tide and waves. The bay is a small semienclosed estuary, located in the high-energy wave environment of the southeastern Bay of Biscay (Figure 1). As a sheltered bay where the currents are generally weak compared to the neighboring exposed nearshore areas, it may be impacted by runoff pollution carried with river inflows. River plumes are characterized by a remarkable stratification in the bay, with freshwater concentrated in a thin surface layer.

[6] The present work focuses on the effect of waves on river plume dynamics and on water exchanges between the bay and the inner shelf. Due to the limited field data set available in the bay for now [*Delpey*, 2012] and the difficulty to use point measurements for the study of complex flows, this paper proposes an analysis based on wave-current numerical modeling, as a first step in the investigation of the complex dynamics of the bay. An original description of main dispersion processes under the effect of wave-current interactions is provided in a realistic configuration with strong 3-D features. Section 2 describes the study site and field data. Wave and current models implementation is given in section 3. An analysis of waves transformation and modeled wave-induced circulation are then provided in section 4, and effects of waves on freshwater dispersion are investigated. Conclusions are summarized in section 5.

2. Study Area and Event of Interest

[7] The bay of Saint Jean de Luz-Ciboure is located in the south of the French Atlantic Coast, 10 km northward from the Spanish border (Figure 1). This region is exposed to energetic swells coming mainly from North Atlantic with direction W-NW. The offshore mean significant wave height and peak period are 1.6 m and 9.6 s, respectively [*Abadie et al*., 2005]. The study site is a shallow mesotidal bay, with tidal range about 4.5 m at spring tides. The bathymetry of the area is presented in Figure 1d. The bay is approximately 2 km long by 1 km wide. The area is semi-enclosed by breakwaters which delimit two inlets connecting the bay with the inner shelf. These shallow inlets with mean depth 13 and 8 m are, respectively, 250 and 350 m wide. The small cross section in the inlets causes the acceleration of tide-induced currents and related mass exchanges between the bay and the inner shelf during the tide cycle. Ocean waves can penetrate in the bay, especially, through the wider eastern inlet. In the northeastern part of the bay, wave breaking is regularly observed over a shallow rocky platform. During energetic events, a high level of wave energy is dissipated in this area. The platform mean depth is about 0.5 m above the Lowest Astronomical Tide (LAT) level, so that a part of it is intertidal when the tidal range is large. The platform surface is rocky and very irregular. Ponctual measurements of rock formations height show that it often reaches several tens of centimeters high (Figure 2). A steep slope connects the platform to the deeper part of the bay, where the bottom is mixed sandy/rocky with gentler slopes.

[8] The bay receives freshwater inflows from two small rivers (Figure 1b). The annual mean flow is 5 $m^3\ s^{-1}$ for the main river (Nivelle river) and of the order of 1 $m^3\ s^{-1}$ for the smaller river. During intense rain events, measurements of bacterial loads (not shown) revealed that both rivers can receive significant inputs of fecal indicator bacteria in runoff from their watersheds. Such contamination process is a common feature in many coastal urban watersheds [e.g., *Fiandrino et al*., 2003; *Reeves et al*., 2004]. These

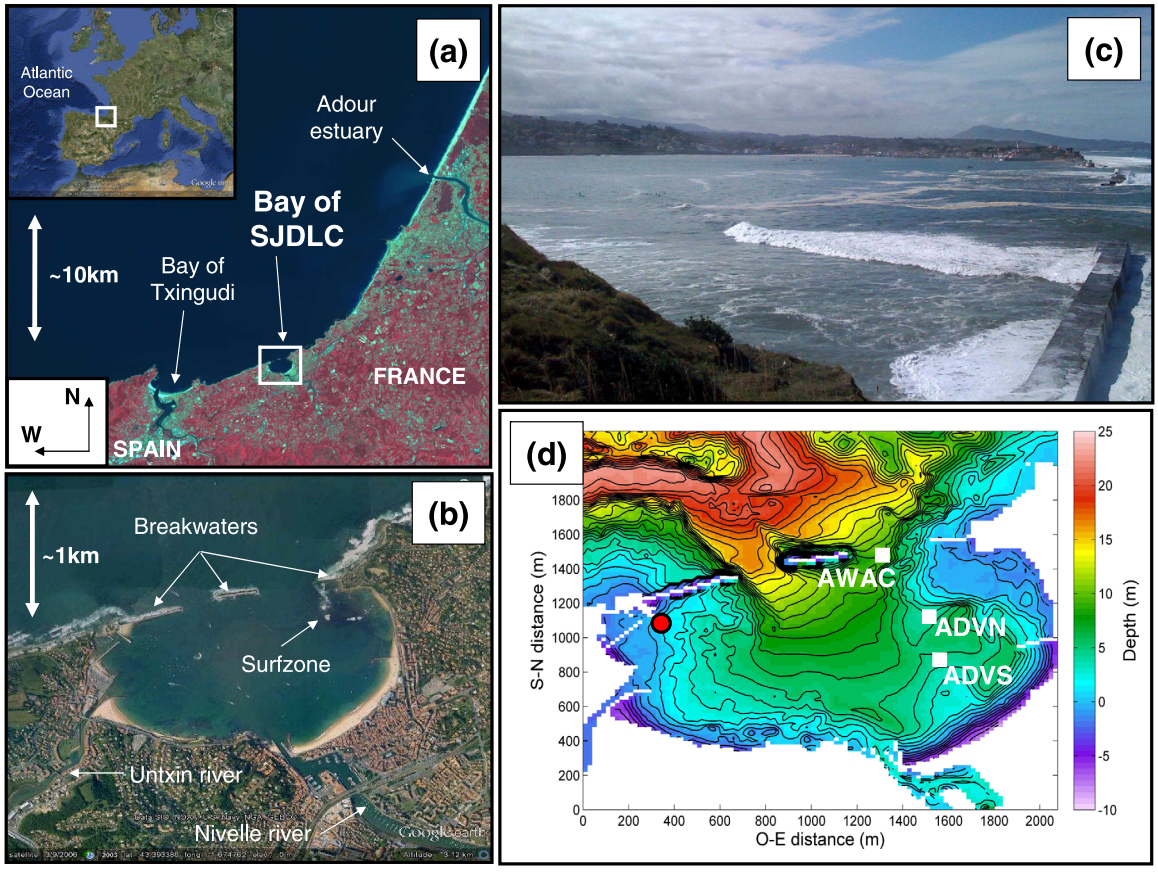

Figure 1. (a) SPOT image of the Atlantic coast on either side of the France-Spain border. SPOT4: 20 m color composite image, 22 July 2008. (b) Aerial photograph of the study site. Google Earth image, Data SIO, NOAA, U.S. Navy, 3 September 2006. (c) Photograph of the bay taken at high tide from the eastern breakwater, with the inlets on the right and the rocky platform surf zone in the center. (d) Bathymetry of the studied bay. Depth is positive downward, relative to the Lowest Astronomical Tide (LAT) level of Saint Jean de Luz harbor. Mean water level is 2.48 m above the LAT level. White squares: wave measurement locations. Red dot: Socoa tide gauge location.

bacterial contaminant are then likely to be introduced into the bay with river inflows. The following dispersion processes and the related impact on water quality are an important issue for the touristic area of Saint Jean de Luz-Ciboure.

[9] In this paper, the bay dynamics are examined during the episode from 22 to 28 September 2010. Environmental conditions encountered during this time interval are plotted in Figure 3. It can be seen that the studied interval corresponds to a river flood event occurring under high-energy wave conditions (max. offshore $H_s \sim 2.5$ m). Wind velocity is also significant on 24 September (>10 m s^{-1}), with N to NW direction. Tidal range varies from 2.5 to 3.3 m over the time period. The bay response to the river outflow under the effect of these different forcings will be investigated. During the studied time interval, field data were collected by three bottom mounted sensors deployed in the framework of LOREA 2010 experiment (Littoral, Ocean, Rivers in Euskadi Aquitain, http://www.lorea.eu/). Sensor locations are indicated in Figure 1d. In the present work, recorded wave data will be used and compared with modeling results. A Nortek Acoustic Waves and Current profiler (AWAC) was settled in the eastern inlet at 9 m depth under the LAT level. It recorded wave data using a sampling frequency $f_s = 2$ Hz. Inside the bay, two Nortek Vectors (hereinafter ADVN and ADVS) were deployed to measure

Figure 2. Photograph taken on the intertidal domain of the rocky platform (northeast of the bay).

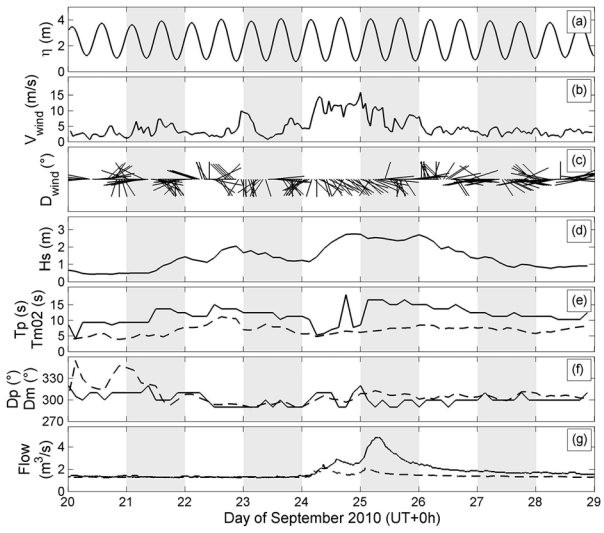

Figure 3. (a) Mean water elevation η measured by Socoa tide gauge inside the bay. (b) Wind velocity V_{wind} and (c) wind direction D_{wind} measured by the Socoa meteorological station (Météo France). Hourly averages of offshore (d) significant wave height H_s, (e) peak period T_p (full line) and mean period T_{m02} (dashed), and (f) peak direction D_p (full line) and mean direction D_m (dashed). Offshore wave data were measured by the Donostia directional buoy, located 30 km off the bay at (−2.0126°E, 43.56°N). (g) Upstream flow of the main (full line) and the secondary (dashed) rivers.

waves in the east part of the bay, close to the surf zone (Figure 1d). The ADVN was deployed southward from the platform, at depth 4 m, in order to provide information about wave refraction and dissipation over the platform. The ADVS was settled farther from the surf zone, also at 4 m depth. The ADVN and ADVS recorded wave data using a sampling frequency $f_s = 4$ and 8 Hz, respectively. Due to a sensor dysfunction, wave data are only available from 25 to 27 September at the ADVS location.

[10] Some point measurements of current velocity and salinity profile were also collected as part of LOREA 2010 deployment. However, given the studied configuration complexity, the present work will not seek for an evaluation of the model ability to reproduce the few available flow measurements, but rather focus on a description of dispersion mechanisms at the scale of the whole bay, based on main processes simulated by the wave-current model. A detailed description of LOREA 2010 experiment and of preliminary flow model-data comparison may be found in *Delpey* [2012].

3. Numerical Modeling

3.1. General Implementation

[11] The studied bay is partially exposed to energetic wave conditions. It is also expected to involve significant effects of the flow vertical structure, related to river plumes dynamics in sheltered areas. To investigate freshwater dispersion in this configuration, a full 3-D wave-current model is used, including a representation of the vertical shear of wave momentum and forcing as well as wave-induced vertical mixing. The present work is based on the coupling of the flow model MOHID Water [*Martins et al*., 2001; *Braunschweig et al*., 2004] and the spectral wave model WAVEWATCHIII® (WWIII) [*Tolman*, 2008, 2009], using the glm2z formulation proposed by *Ardhuin et al*. [2008b].

[12] To predict wave-current dynamics inside the bay, the computation is carried out on three nested domains, represented in Figure 4. Offshore wave conditions are first propagated up to the vicinity of the bay on domain G1. The domain extends approximately 30 km off the bay. The corresponding computational grid is regular with size 412 by 286 and mesh steps 100 m. Waves and current are then computed on two nested levels with refined grids (G2 and G3), from approximately 20 m mean depth to the shoreline inside the bay. The second level G2 aims at providing river inflows forcing for the level G3. The flow is computed along the tidal section of both rivers up to the bay. To allow a realistic modeling of these very narrow sections with a limited grid size, a variable mesh step is adopted in G2-grid, from 100 m steps offshore to 20 m steps over the rivers upstream section. The total number of grid points is 208 by 155. The solution of level G2 is transmitted at open boundaries of the last level G3 (in particular flow properties at river outlets). The domain G3 covers the bay area, with an offshore boundary located 1 km off the bay inlets. Wave computation is carried out on a 246 by 260 regular grid with 10 m steps. Wave forcing terms are then interpolated on a 123 by 130 regular grid with 20 m mesh steps for the flow computation. In levels G2 and G3, the flow model vertical discretization uses 10 sigma levels, with finer resolution close to the surface and at the bottom.

[13] Bathymetry of level G1 was derived from data provided by the French Navy Hydrographic and Oceanographic Service (SHOM). For levels G2 and G3, a compilation of bathymetric and topographic surveys data was provided in the framework of the LOREA project. Horizontal resolution of these data ranges from 1 m (in the deeper parts of the domain) to approximately 20 m (in most of the shallow areas like the rocky platform, the intertidal domain, river sections).

3.2. Wave Model Implementation

[14] Wave transformation is simulated with the spectral wave model WWIII in its version 4.04 [*Tolman*, 2008, 2009]. WWIII has been widely validated at global and regional scales [e.g., *Tolman*, 2002; *Ardhuin et al*., 2008a, 2010], and more recently in nearshore areas [e.g., *Filipot*

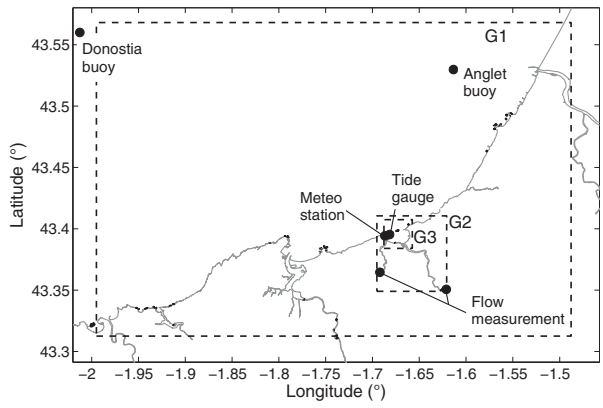

Figure 4. Coastline (gray line), computational domains (black dashed line), and data locations (black points).

and Ardhuin, 2012; *Michaud et al*., 2012; *Ardhuin et al*., 2012]. The model solves the spectral balance equation for the wave action density N, with source terms S_{in}, S_{nl}, S_{oc}, and S_{bot} for wind input, nonlinear four-waves interactions, wave breaking dissipation and bottom friction dissipation, respectively. The term S_{oc} is considered as the sum of two contributions S_{ds} and S_{db}, respectively, for whitecapping and depth-induced breaking in very shallow water. Triad interactions and bottom scattering effects are not taken into account in the present study.

[15] The wind-wave generation and dissipation (terms S_{in} and S_{ds}) are parameterized according to *Bidlot et al*. [2005]. Nonlinear four-waves interactions are modeled using the Discrete Interaction Approximation (DIA) as proposed by *Hasselmann et al*. [1985]. In shallow areas, like the bay studied here, wave energy dissipations by bottom friction and depth-induced breaking become very important, and S_{bot} and S_{db} are much larger than the whitecapping dissipation term S_{ds}. Parameterization of the bottom friction dissipation term S_{bot} uses the linear JONSWAP formulation [*Hasselmann et al*., 1973], given by

$$S_{bot}(\mathbf{k}) = -\Gamma\left[\frac{2\pi f}{g\sinh(kD)}\right]^2 E(\mathbf{k}), \tag{1}$$

where $\mathbf{k}$ is the wave number vector, f is the frequency, g is the gravity acceleration, D is the water column height, $E = 2\pi f N$ is the wave energy density spectrum, and Γ is a constant friction coefficient. Depth-induced breaking dissipation is parameterized according to *Battjes and Janssen* [1978]. Wave heights are limited by the threshold height $H_{max} = \gamma D$, with a constant breaker parameter γ. The dissipation term S_{db} due to depth-induced breaking is given by

$$S_{db}(\mathbf{k}) = -0.25 Q_b f_m \frac{H_{max}^2}{E_{tot}} E(\mathbf{k}), \tag{2}$$

where Q_b is the breaking probability of the random sea state, f_m is the mean frequency and $E_{tot} = \int_{\mathbf{k}} E(\mathbf{k})\mathrm{d}\mathbf{k}$. For the present application, values of parameters Γ and γ were adjusted based on wave model-data comparison, as further discussed in section 4.1.

[16] Wave spectra are discretized over 25 frequencies exponentially spaced from 0.041 to 0.41 Hz so that two successive frequencies f_i and f_{i+1} are related by $f_{i+1} = 1.1 f_i$, and 36 directions with a constant 10° directional resolution. Offshore wave conditions are obtained from hourly directional spectra provided by the Donostia buoy (depth 450 m), located 30 km off the bay at (−2.0126°E, 43.56°N) (Figure 4). On the three computational levels G1 to G3, surface elevation is prescribed from the 10 min record of the Socoa tide gauge and wind forcing is given by the hourly measurement of the Socoa meteorological station (see Figure 4). The current retroaction on waves is not taken into account in this study.

3.3. Flow Model Implementation

[17] The present work is based on the code MOHID, a 3-D baroclinic, incompressible (Boussinesq), hydrostatic, and free-surface ocean model. MOHID uses a finite volume method to discretize governing equations in a structured C-grid and a semi-implicit (ADI) temporal algorithm. Equations are numerically solved by the model with a procedure equivalent to a generic vertical coordinate [*Martins et al*., 2001], allowing for different types of vertical discretization, like the sigma coordinate used for the present study. The numerical procedure allows a representation of the wetting and drying of intertidal regions. MOHID system is coupled to the General Ocean Turbulence Model (GOTM) [*Burchard and Bolding*, 2001] for the vertical turbulent closure. Detailed description of the code implementation can be found in *Montero* [1999] and *Martins et al*. [2001]. The MOHID hydrodynamic model has been used successfully in complex ocean and coastal applications [e.g., *Martins et al*., 2001; *Coelho et al*., 2002; *Leitão et al*., 2005; *Malhadas et al*., 2009] and compared well with several state-of-the-art ocean models in the Bay of Biscay [*Riflet et al*., 2010].

[18] The model used in the present study, further referred to as "MOHID-GLM," is a new MOHID version modified to allow a full 3-D modeling of the mean flow including the effects of waves, with all other elements retained from the original MOHID code. The new code version solves the glm2z asymptotic formulation of the GLM wave-current equations for the quasi-Eulerian momentum, as proposed by *Ardhuin et al*. [2008b] and further adapted by *Bennis et al*. [2011]. The quasi-Eulerian velocity field, noted $\hat{\mathbf{u}} = (\hat{u}_1, \hat{u}_2, \hat{w})$, is defined as [*Jenkins*, 1989]

$$(\hat{u}_1, \hat{u}_2, \hat{w}) = (\overline{u}_1^L, \overline{u}_2^L, \overline{w}^L) - (u_1^S, u_2^S, w^S), \tag{3}$$

where $\overline{\mathbf{u}}^{\mathbf{L}} = (\overline{u}_1^L, \overline{u}_2^L, \overline{w}^L)$ is the Lagrangian mean velocity field and $\mathbf{u}^{\mathbf{S}} = (u_1^S, u_2^S, w^S)$ is the Stokes drift velocity field. The vertical coordinate change used by *Ardhuin et al*. [2008b] corrects the vertical coordinate so that the glm2z equations are nondivergent. The reader is referred to Appendix A for a presentation of the complete set of equations solved by MOHID-GLM, and to *Delpey* [2012] for a detailed description of the code implementation.

[19] MOHID-GLM is coupled with a $\mathcal{K}-\epsilon$ model [*Rodi*, 1980] to determine the vertical eddy viscosity and diffusivity coefficients in the momentum and tracer conservation equations. To account for the wave-enhanced vertical mixing at the surface [*Agrawal et al*., 1992; *Terray et al*., 1996; *Feddersen*, 2012a, 2012b], a wave-induced surface TKE flux is introduced in the surface boundary conditions of the $\mathcal{K}-\epsilon$ scheme, and an enhanced surface roughness length $z_{0,s}$ is used [*Craig and Banner*, 1994]. As proposed by *Terray et al*. [1996, 2000], $z_{0,s}$ is considered proportional to the total significant wave height H_S, i.e., $z_{0,s} = \alpha_0 H_S$, with α_0 a constant. Here the value $\alpha_0 = 0.6$, proposed by *Soloviev and Lukas* [2003], was adopted. For the horizontal mixing, a constant horizontal eddy viscosity K_H was used and set to $K_H = 1.0\ \mathrm{m^2\ s^{-1}}$ (see Appendix A).

[20] The importance of bottom friction for wave-induced surf zone currents has been demonstrated by several authors, especially in the longshore direction [e.g., *Longuet-Higgins*, 1970a, 1970b; *Thornton and Guza*, 1986]. In the present work, the specification of the bottom roughness length $z_{0,b}$ also appeared critical to the determination of wave-induced currents in the surf zone. This parameter is spatialized in order to account for the variable nature of the

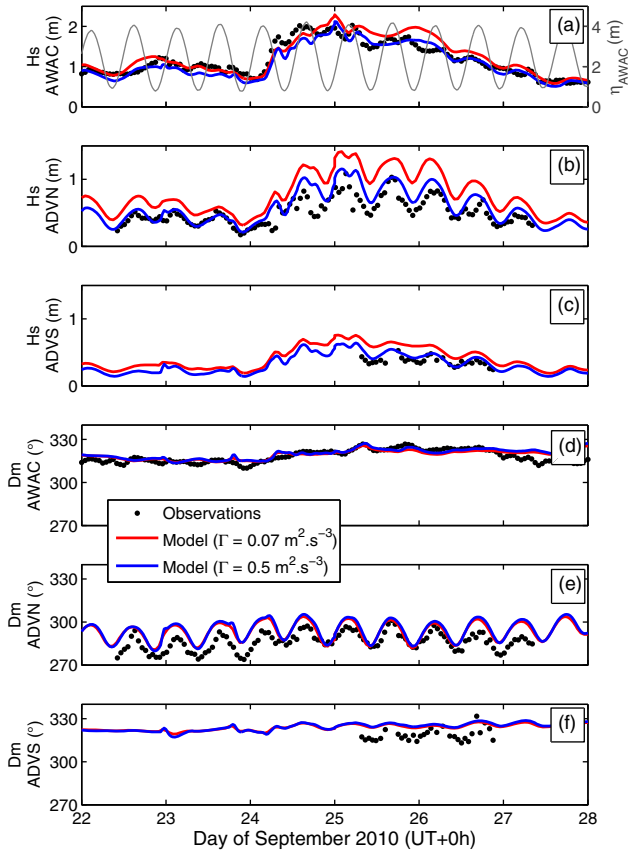

Figure 5. Observed and modeled time series of hourly averaged wave height H_s at the (a) AWAC, (b) ADVN, and (c) ADVS location. Water level recorded by the AWAC is also plotted (gray line) in Figure 5a. Observed and modeled time series of hourly averaged mean direction D_m at the (d) AWAC, (e) ADVN, and (f) ADVS location. Modeled results are shown for two different bottom friction coefficients: the default value $\Gamma = 0.07$ m^2 s^{-3} (red) and the selected value $\Gamma = 0.5$ m^2 s^{-3} (blue).

bottom in the studied site: for relatively smooth sandy areas, $z_{0,b}$ was set to 0.001 m, and for very rough rocky areas, a maximum value $z_{0,b} = 0.1$ m was used. This latter value of $z_{0,b}$ is large compared to more often cited values for sandy bottoms, which range usually from 0.001 to 0.01 m [e.g., *Weir et al.*, 2011]. Frictional dissipation over rocky seabeds has been less studied [*Nunes and Pawlak*, 2008]. In the present configuration, the value of $z_{0,b}$ in the rocky area was adjusted to meet a qualitative consistency of model results with preliminary flow measurements available in the bay (not shown). The adopted schematic parameterization of $z_{0,b}$ may be seen as a first attempt to account for the unusually large roughness of the rocky platform (Figure 2). However, as a tunable parameter, the selected high $z_{0,b}$ value may also compensate for other unknown sources of errors. As part of further work, a quantitative analysis of the roughness elements distribution over the rocky area would be required to improve the representation of this feature.

[21] For the flow computation on domain G2, surface elevations are prescribed at the offshore boundary from the 10 min measurements of the Socoa tide gauge. The flow of each river is prescribed from in situ measurements at an upstream location, where the influence of tidal oscillations on the flow is negligible (see Figure 4). The flow is then computed along the tidal section of both rivers, which is approximately 6 km long for the main river and 3.5 km long for the secondary river. At the most refined level G3, open boundary conditions are imposed by the solution of level G2. Both domains are forced by a homogeneous wind field, given by the hourly record of the Socoa meteorological station (Figure 4). Finally, wave related terms required for the flow calculation are computed by WWIII from the wave field and transmitted to MOHID-GLM every 30 min.

4. Results

4.1. Wave Transformation

[22] Wave transformation inside the bay is examined during the time interval from 22 to 28 September. Model results are compared with field data from the Anglet buoy (Figure 4) and from the three bottom mounted sensors deployed in the bay at this time (see section 2).

[23] Figure 5 shows observed and simulated time series of significant wave height H_s and mean direction D_m at the AWAC, ADVN, and ADVS locations. Measurements from the AWAC allow us to identify two different wave events, for which frequency spectra are plotted in Figure 6: (1) low-energy waves from 22 to 24 September with $H_s \sim 1$ m, $T_p \sim 10$ s, and $D_m \sim 315°$ and (2) a more energetic sea state with maximum $H_s \sim 2$ m and mean direction $D_m \sim 325°$ from 24 to 28 September, which consisted in a very long swell with $T_p \sim 20$ s superimposed to a shorter wave system with $T_p \sim 7$ s. Inside the bay, a strong decrease of

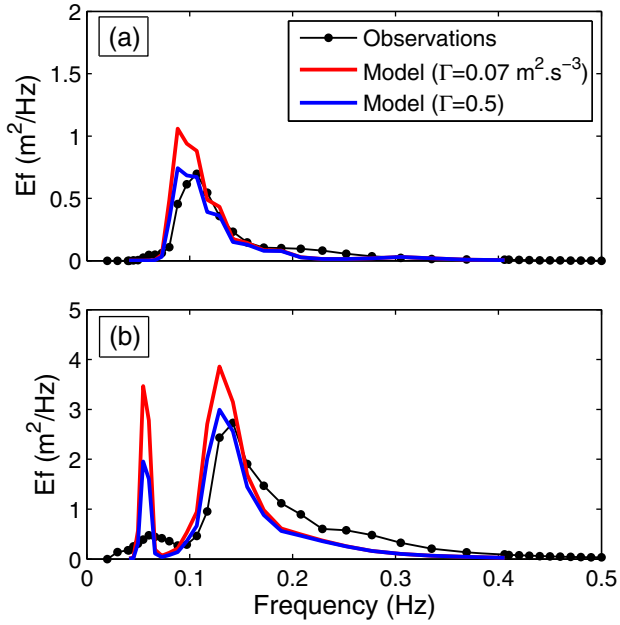

Figure 6. Hourly averaged frequency spectra E_f at the AWAC location from field data (black), model with the default (red) and selected (blue) friction coefficient (a) during the low-energy wave event (23 September at 16:00) and (b) during the high-energy wave event (25 September at 00:00).

wave energy is observed (ADVN,S), related to important modifications of waves when propagating in the shallow eastern part of the bay. First, waves are refracted over the S-N oriented isobaths of the rocky platform. It causes wave direction to shift from incident values between 310° and 330° (AWAC) to directions ranging from 275° to 300° on the ADVN (Figures 5d and 5e). Second, wave energy is dissipated over the rocky platform, due to depth-induced breaking and bottom friction. The ADVN time series also shows that wave transformation over the platform is strongly modulated by the water level. Measured H_s at the ADVN location are approximately two times higher at high tide than at low tide. The direction shift due to refraction appears larger at low tide by 10°–20° compared to high tide.

[24] For the wave simulation, the breaking parameter γ and the wave friction coefficient Γ were adjusted to (γ, Γ) = (0.75, 0.5 $m^2\ s^{-3}$) on refined levels based on comparison of WWIII results with wave data recorded by the AWAC and the ADVN,S. Results obtained with selected parameters compare reasonably with field data during the 6 days interval examined here, for both low and high-energy conditions. Γ is essentially a tuning parameter here, correcting for all possible errors in the definition of the offshore boundary conditions, and necessary to produce reasonable wave parameters in the bay. The reader is referred to Appendix B for an additional discussion of this aspect and of other wave model parameters and error statistics.

4.2. Wave-Induced Circulation in the Bay

[25] Wave fields computed by the WWIII model are now used to force the 3-D flow model calculation on the study area. Results of the wave-current modeling are examined during the time interval from 22 to 28 September 2010, in order to illuminate the main features of the bay circulation in response to the different nearshore forcings. Special attention is given to the effects of the increase in incident wave energy on 24 September, in order to further investigate the related impact on freshwater dynamics in the bay (next paragraphs). MOHID-GLM has been successfully validated and compared to reference wave-current models on simplified nearshore configurations [see *Delpey*, 2012], so that its ability to capture nearshore processes can be expected. The present work is a first step in the small-scale application of such a 3-D wave-current model to study a complex realistic circulation in a stratified environment, under both low and high-energy wave conditions.

[26] Figure 7 shows the surface Lagrangian mean velocity field computed by the model at three different instants of the examined time interval: during the low-energy wave episode at low tide (Figure 7a), and during the high-energy wave episode at high tide (Figure 7b) and at low tide (Figure 7c). As expected in the studied mesotidal environment, model results show a significant role of tide in the bay circulation. In particular, the small cross section of the inlets and of both river mouths causes the acceleration of barotropic tidal currents, leading to mass exchanges between the rivers, the bay and the inner shelf. However, in addition to the tidal circulation, the wave-current modeling also suggests a remarkable role of waves in the circulation patterns inside the bay. Due to the angle between incident wave

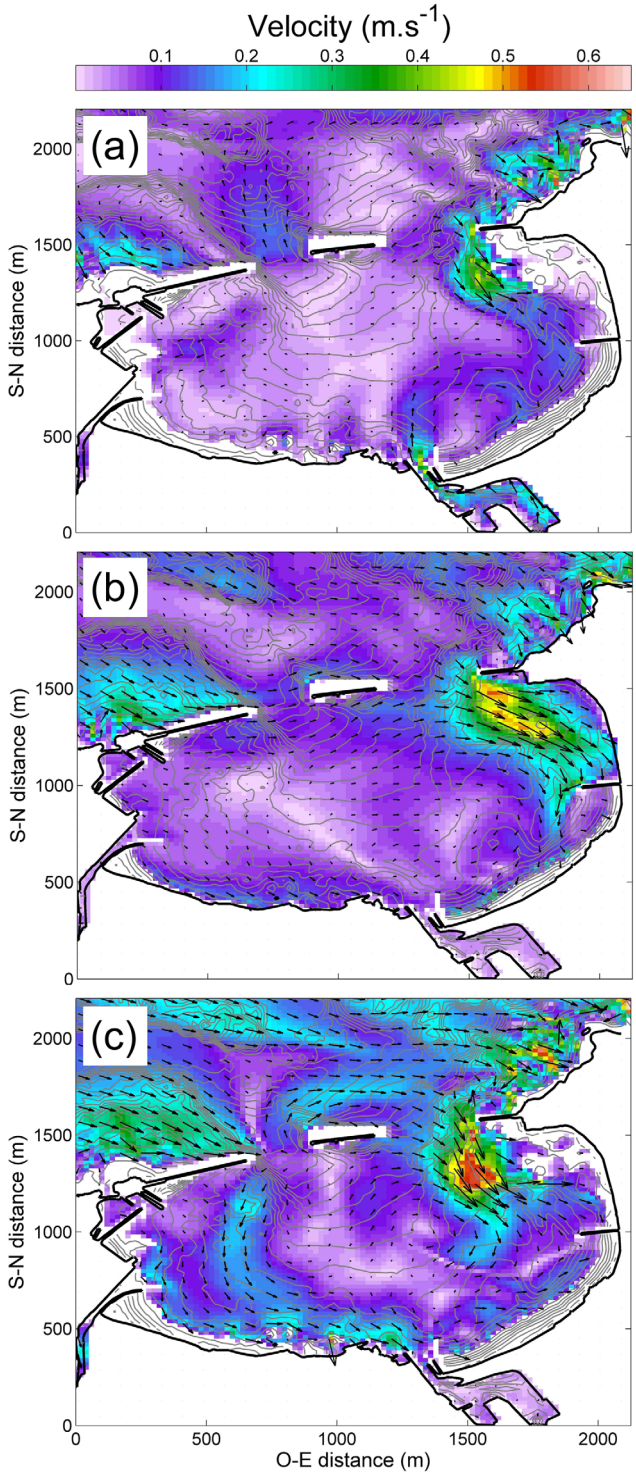

Figure 7. Modeled surface Lagrangian mean velocity on 23 September 2010 at (a) 09:00 (low tide) and on 24 September 2010 at (b) 16:00 (high tide), and (c) 23:00 (low tide). Velocity fields are averaged over the top 20% of the water column. The colorscale indicates the velocity modulus. Isobaths are superimposed in gray every 1 m.

direction and the orientation of the rocky platform isobaths in the northeastern part of the bay (Figures 1 and 5), wave breaking over the platform generates a longshore current with south to southeastward direction. This feature is in

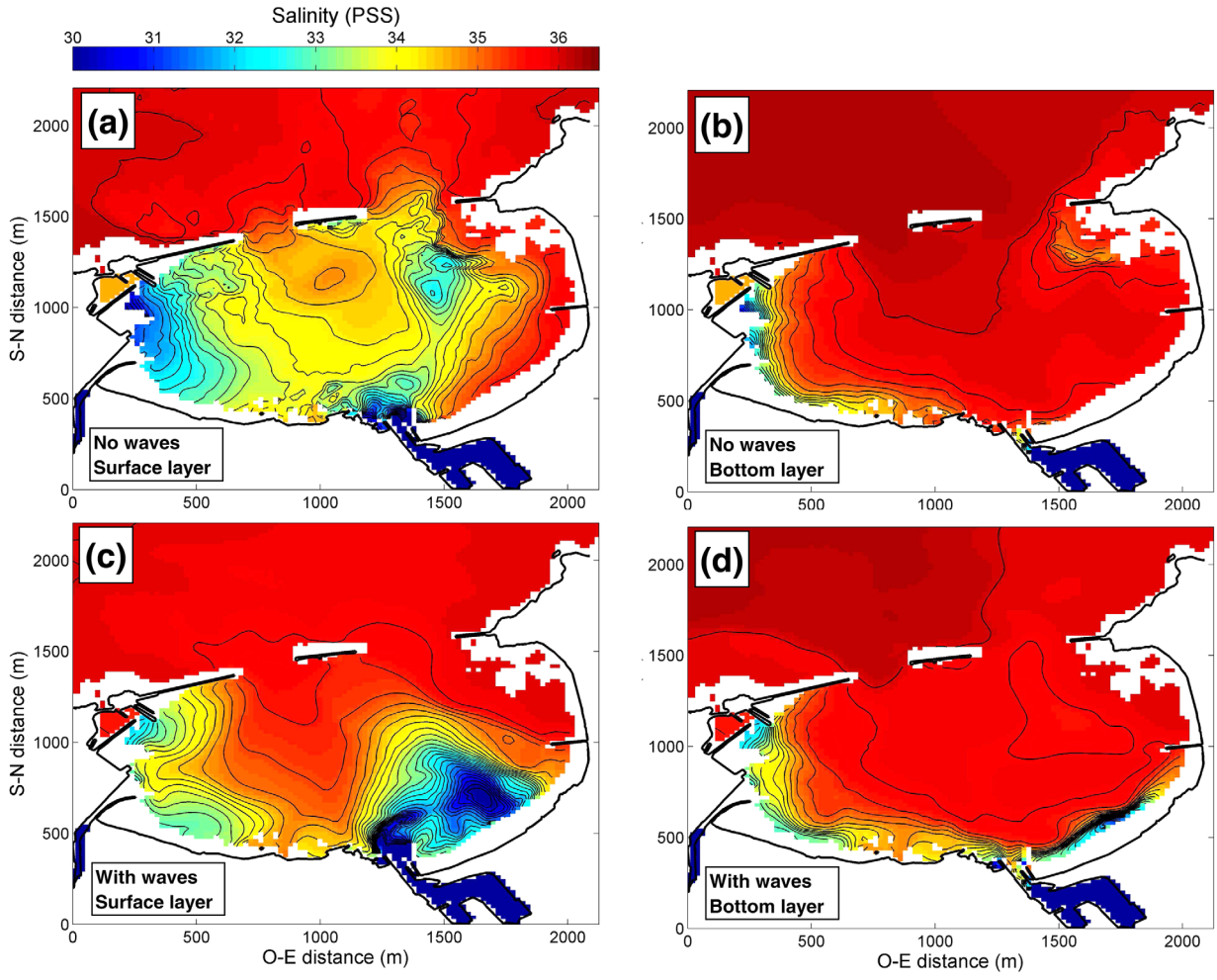

Figure 8. Fields of modeled salinity at low tide during the high-energy wave episode (26 September at 11:00) (a, b) without and (c, d) with wave forcing activated. (a, c) Average over the top 20% of the water column and (b, d) average over the lowest 20% of the water column.

agreement with the relatively well known generation mechanism first exposed by *Longuet-Higgins* [1970a, 1970b]. The intensity of the wave-induced longshore current in the surf zone is important compared to the slower circulation in the rest of the bay. The existence of this surf zone current was consistent with a pilot drifter experiment performed in the bay in conditions very similar to 23 September shown in Figure 7a. An alongshore current was visually observed during the experiment with approximately the same location and intensity as in the model.

[27] Surface velocity fields in Figures 7b and 7c illustrate the longshore current dependence on the mean water level. For a given incident wave height and direction, a decrease in the mean water level results in a displacement of the maximum wave dissipation by breaking toward the southwestern deeper part of the platform. As a consequence, the location of the induced longshore current also moves southwestward (Figure 7c). Conversely, an increase in the mean water level induces a displacement of the longshore current location toward the northeastern shallower part of the platform (Figure 7b), which results in a strong tidal modulation of the wave-induced surf zone current. Figures 7a and 7c illustrate the correlation between the longshore current intensity and the incident wave heights. Moreover, comparison of Figure 7a and Figure 7c shows that for a given water level, the location of the longshore current also moves southwestward when incident wave heights increase, as wave breaking occurs in the deeper western part of the platform, bringing another contribution to the variability of the eastern bay circulation.

4.3. Freshwater Dynamics

4.3.1. River Plume Dispersion in the Bay

[28] We focus on the time frame from 22 to 28 September 2010. Figure 8 gives salinity fields obtained from the 3-D wave-current model at low tide during both the high-energy wave episode and the river flood event. To illustrate the effect of waves on river plume dispersion, a model simulation is also performed without taking wave forcing into account. Results are given with (Figures 8c and 8d) and without (Figures 8a and 8b) wave forcing for both surface (Figures 8a and 8c) and bottom (Figures 8b and 8d) water column layers.

[29] In both simulations, the presence of the river plumes results in a thin surface layer with lower salinity and typical depth between 1 and 2 m. This important stratification

produced by the 3-D model is consistent with the few salinity profile measurements collected in the bay (not shown, see *Delpey* [2012]). Salinity fields exhibit a significant space-time variability along the tide cycle, related to varying river outflows and to the following freshwater dispersion and mixing under the effect of the circulation.

[30] Comparison of model results with and without wave forcing suggests a significant effect of waves on the salinity field. The freshwater plume from the main river, in the eastern half of the bay, is particularly affected by wave-induced circulation (Figures 8a versus 8c). The surf zone longshore current over the rocky platform tends to advect salt water into the northeastern part of the bay and thus to push freshwaters southward. It results in an accumulation of freshwater close to the main river mouth. Also, the vertical mixing over the rocky platform is higher with waves, due to the TKE surface flux induced by wave breaking. It contributes to increase the surface salinities in the northeastern area by mixing the surface freshwater with the underlying ocean water. Without wave forcing, a larger northward and eastward spreading of the river plume is obtained in the surface layer, with stronger stratification close to the rocky platform. Moreover, comparison of Figures 8a and 8c shows that a higher freshwater outflow occurs through the bay inlets when wave forcing is not taken into account.

[31] As illustrated by Figure 8, model results suggest a significant modification of freshwater distribution inside the bay due to the asymmetric forcing of the longshore current on the bay circulation. Despite its restriction to the confined and shallow surf zone area, the current induced by wave breaking is much stronger than the slower tide- and wind-induced circulations in the bay (especially at low tide), so that the transport initiated in the surf zone affects freshwater outflow through the bay inlets. This suggests that the wave-induced circulation could also impact freshwater exchanges between the bay and the inner shelf. This feature is now examined.

4.3.2. Freshwater Balance Under the Effect of Waves

[32] In the context of contamination processes related to river outflows, it is interesting to examine how different forcings, here tides, winds, and waves, affect the ability of the bay to evacuate freshwaters. Despite the complexity of the small-scale flow patterns inside the bay, the representation of the different processes by the wave-current 3-D model can be used to draw tendencies in the local freshwater balance in response to a rainfall event. Here the computed salinity is used to establish the balance of river waters inside the bay during the time interval from 22 to 28 September. As mentioned previously, this interval corresponds to a river flood event occurring under high-energy wave conditions (see Figure 3). The total salt quantity in the bay $Q_{s,\mathrm{tot}}$ can be obtained by mixing a volume V_s of ocean water with salinity S_s and a volume V_f of freshwater, so that $Q_{s,\mathrm{tot}} = V_s S_s$. Introducing the total water volume in the bay $V_{\mathrm{tot}} = V_s + V_f$, an equivalent freshwater volume (EFV) can be estimated by

$$V_f = V_{\mathrm{tot}} - \frac{Q_{s,\mathrm{tot}}}{S_s}. \tag{4}$$

[33] The EFV is computed from model results based on four simulations: (1) a wave-current simulation with all forcings, (2) a model simulation with wave forcing switched off, (3) a wave-current simulation with wind forcing on the flow switched off, and (4) a wave-current simulation without Stokes drift contribution, i.e., with $\mathbf{u}^{\mathbf{S}} = \mathbf{0}$. The EFV time series for the four simulations are plotted in Figure 9, together with time series of the wind speed, the incident wave height H_s and the sum of the two river flows. In Figure 9b, the instantaneous EFV (dashed) are superimposed to a residual EFV (full lines) estimated by applying a 24 h 50 min average sliding window. Finally, the time derivative of this residual EFV is plotted in Figure 9c. The water flux $d(EFV)/dt$ gives the overall freshwater flow into the bay, which equals the sum of freshwater fluxes through the two inlets and through the two river outlets.

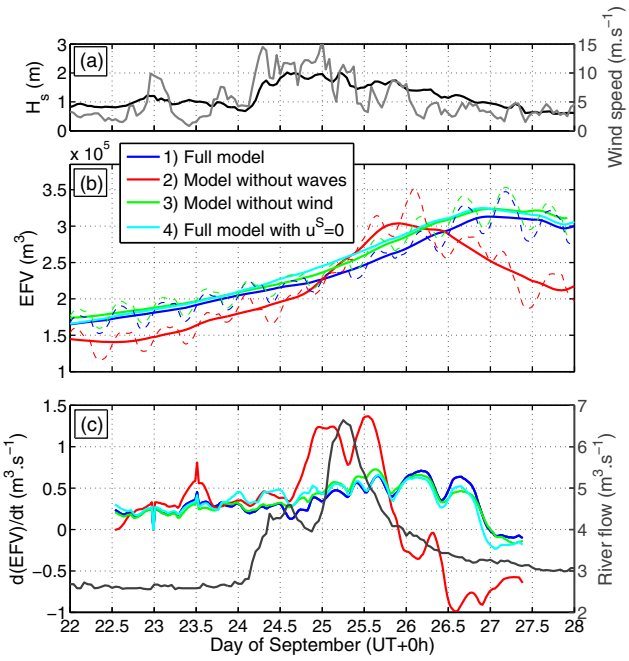

Figure 9. Time series of (a) the wave height H_S measured by the AWAC (black) and the wind speed (gray); (b) the instantaneous (dashed) and the residual (full line) EFV; and (c) the time derivative of the residual EFV (colored) and the sum of the two river flows (gray).

[34] The comparison of simulations 1 and 3 suggests that the wind has little effects on the freshwater balance inside the bay during the examined time period, although the wind speed exceeds 10 m s^{-1} on 24 September. On the contrary, the comparison of simulations 1 and 2 suggests a significant effect of waves on the freshwater balance. The computed EFV is higher in simulation 1 than in simulation 2 at the end of the river flood event on 28 September (Figure 9b). Following the increase in the river flow (on 24 September), results of simulation 2 show a clearly correlated response of the bay to this freshwater input. An increase of the EFV is first obtained, followed by a compensating decrease starting less than 16 h after the peak of the river flood. In simulation 1, the increase in the EFV is slower but with a longer duration. The EFV decreasing phase only starts at the end of the examined time interval, i.e., more than 40 h after the peak of the river flood, when incident wave height H_s becomes lower than 1 m. Thus,

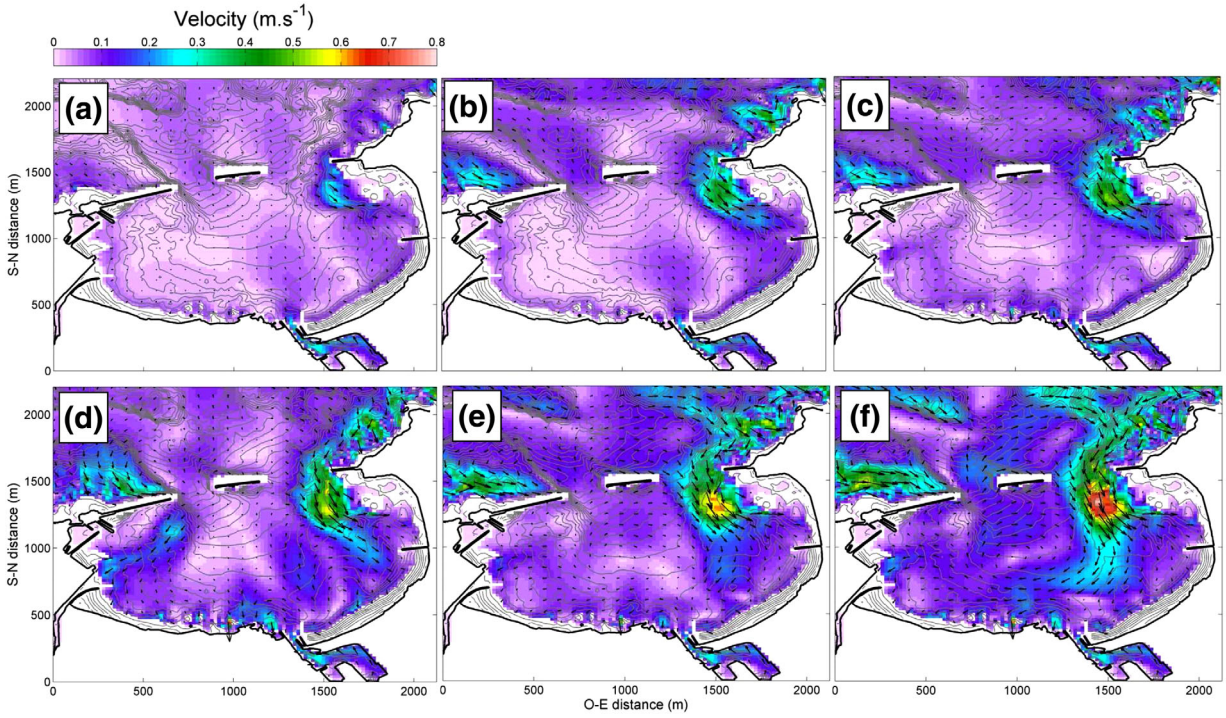

Figure 10. Modeled surface Lagrangian mean velocity during ebb tide of day 2 for (a) (H_s, θ_p) = (0.5 m, 310°), (b) (H_s, θ_p) = (2 m, 280°), (c) (H_s, θ_p) = (2 m, 310°), (d) (H_s, θ_p) = (2 m, 340°), (e) (H_s, θ_p) = (3 m, 310°), and (f) (H_s, θ_p) = (4 m, 310°). Velocity fields are averaged over the top 20% of the water column.

compared to simulation 2, a delay of approximately 24 h is obtained for the EFV flux to become negative. At the end of the river flood event, the EFV in simulation 1 is about 40% higher than in simulation 2. The freshwater outflow on 27 September is of the order of 0.1 m^3 s^{-1} with waves, which is still much lower than the 0.5 m^3 s^{-1} outflow obtained without waves.

[35] The obtained tendencies suggest that waves contribute to maintain freshwaters inside the bay. Although the EFV increases faster without waves at the peak of the river flood event, at the end of this event, a higher volume of freshwater is retained inside the bay due to wave forcing. Waves delay the evacuation of this volume and limit the freshwater outflow until low-energy conditions are met. An additional experiment performed in the wave case confirms that the extra freshwater volume retained in the bay would be subsequently evacuated from 28 to 30 September if very low-energy waves were encountered during this time interval (not shown). The Lagrangian transport by waves (Stokes transport) could be a possible driving factor of freshwater retention in the bay. However, a simulation with Stokes transport turned off (Figure 9, light blue lines) shows that the Stokes drift has little contribution in the present configuration. This result suggests that the outflow reduction is mainly due to the wave-induced longshore current in the eastern bay surf zone. It generates a transport oriented toward the inner bay, in opposition with tidal currents during ebb tide. This reduces the primary outflow of freshwater through the eastern inlet (also illustrated in Figure 8), yielding a reduction of the bay flushing during the examined time interval.

4.3.3. Freshwater Balance Sensitivity to Incident Wave Characteristics and Longshore Current Velocity

[36] To investigate the variability of the bay flushing with incident wave characteristics, the modeled bay dynamics is now examined in a simplified configuration under different offshore wave conditions. Simulations are performed using a sinusoidal tidal forcing of the water level with period 12 h 25 min (corresponding to the dominant M2 component) and a constant 3 m tidal range. Wind forcing is switched off and upstream river flows are constant, set to 2.5 m^3 s^{-1} for the main river and 0 m^3 s^{-1} for the secondary river. At the offshore boundary of the domain G1 (Figure 4), constant wave conditions are prescribed by a JONSWAP spectrum. First to investigate the effect of incident wave energy, simulations are carried out using an offshore peak period T_p = 10 s, peak direction θ_p = 310°, and significant wave height H_s in {0.5, 1, 2, 3, and 4 m}. Second to investigate the effect of incident wave direction, simulations are carried out with offshore T_p = 10 s, H_s = 2 m, and θ_p in {280°, 340°}. Finally, a simulation is also performed with wave forcing switched off. The flow model computation is initialized without wave forcing. Waves are then introduced at day 0 and the subsequent bay response is examined. Figure 10 shows the surface Lagrangian mean velocity field computed by the model for different offshore wave conditions at the same time instant, during ebb tide of day 2. In addition, Figure 11 represents the maximum velocity V_{max} of the longshore current over the simulated time interval, as a function of the offshore wave height H_s. Finally, residual EFV obtained from the ensemble of simulations are plotted in Figure 12.

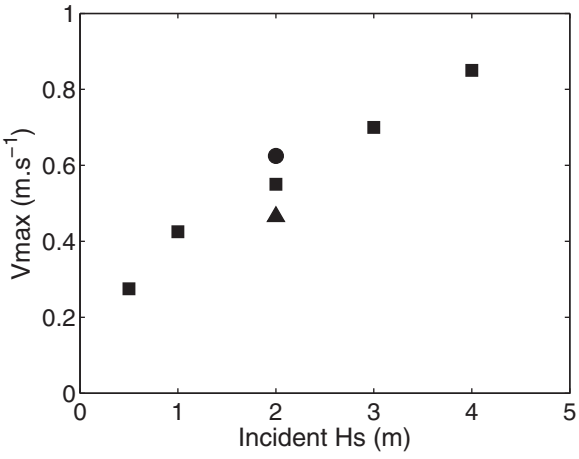

Figure 11. Maximum velocity $V_{\max}$ of the wave-induced longshore current over the simulated time interval for the different offshore wave conditions. Black squares correspond to conditions with $\theta_p = 310°$, the black triangle and circle correspond to $\theta_p = 280°$ and $\theta_p = 340°$, respectively.

[37] Figure 12b shows that simulation without waves (black line) gives a nearly constant residual EFV during the examined time interval. This results from the equilibrium between tidal and river inflow forcings. Considering wave cases with offshore $H_s = 1$ m and $H_s = 2$ m (Figure 12b, red and light blue lines), a comparable EFV increase of approximately 40% is obtained at day 2, consistent with results from the realistic simulation exposed in the previous section. With offshore $H_s = 0.5$ m (dark blue line), the residual EFV is lower than with H_s between 1 and 2 m by approximately 15%. Figures 10a and 11 show that this EFV reduction is correlated with a reduction of the longshore current intensity $V_{\max}$, due to lower incident wave energy (for a given incident direction). Conversely, Figures 10e, 10f, and 11 illustrate the increase in $V_{\max}$ with higher incident wave energy $H_s = 3$ and 4 m compared to $H_s = 2$ m. However, a further increase in the residual EFV with $V_{\max}$ is not obtained for $H_s > 2$ m. The wave-induced EFV at day 2 is lower by 10% for $H_s = 3$ m (Figure 12b, green line) and by 25% for $H_s = 4$ m (purple line), compared to the case with $H_s = 2$ m.

[38] With smaller differences, the same tendency is obtained when examining the different incident wave directions with $H_s = 2$ m. Figures 10b, 10d, and 11 show an increase in $V_{\max}$ with the incident wave direction. This feature relates to the dependence of the longshore current velocity on the angle between incident waves and the S-N-oriented isobaths of the rocky platform. A larger angle (i.e., norther incoming waves) generates a stronger longshore current. However, examining Figure 12b shows that this stronger current does not result in a higher EFV at the end of the simulation: the EFV is slightly lower for N/NW incident direction (red circles) than for NW and W/NW direction (red line and red squares).

[39] To further investigate the relationship between $V_{\max}$ and freshwater exchanges with the inner shelf, freshwater fluxes through the bay inlets are now examined. Considering that the total water flux F_{tot} through one inlet cross-section results from the sum of a flux F_s of ocean water with salinity S_s and a flux F_f of freshwater, an equivalent freshwater flux through the inlet cross section can be estimated from the model by

$$F_f = F_{\text{tot}} \frac{S_s - S}{S_s}. \tag{5}$$

Then integrating this flux over the simulated time interval, the total freshwater volume (or EFV) exchanged through the considered inlet is computed. The flux F_f and the corresponding EFV exchange are counted positively when entering the bay and negatively when directed seaward. Figure 13 gives the total EFV exchange during the simulated time interval partitioned into each inlet (Figure 13b) and through both inlets (Figure 13c, sum of EFV exchanges through both inlets). In addition, Figure 13a shows the residual EFV in the bay at day 2. All of these freshwater volumes are plotted as a function of the maximum velocity $V_{\max}$ of the wave-induced longshore current over the rocky platform. The value $V_{\max} = 0$ is used to represent the no wave case.

[40] Figure 13a shows the increase in the freshwater volume retained inside the bay for $V_{\max}$ lower than approximately 0.6 m s^{-1}. This corresponds to $H_s < 2$ m for NW incident waves. In consistency with the mechanism suggested previously, Figure 13b shows that under these wave conditions, the wave-induced transport initiated in the surf zone reduces the primary freshwater outflow through the eastern inlet. At the same time, a larger EFV is evacuated through the western inlet. However, Figure 13c suggests that this western outflow increase does not compensate the eastern outflow reduction, as the sum of the EFV exchanges through both inlets increases (reminding that it is counted negatively seaward). This results in freshwater retention inside the bay, with an increased residual EFV in the bay at day 2 of the simulation.

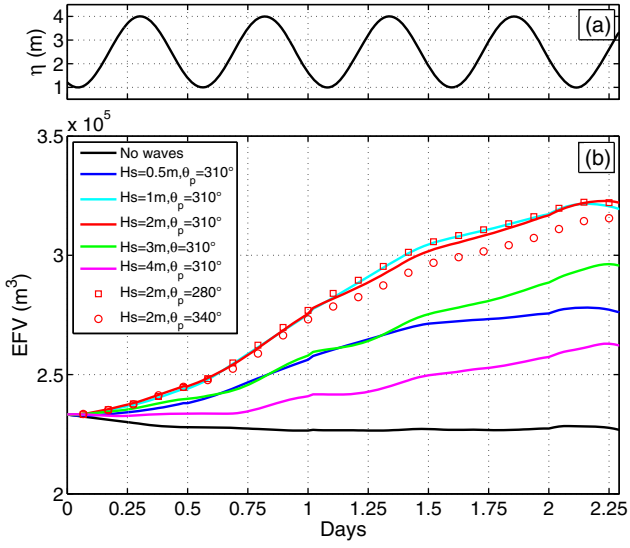

Figure 12. Time series of (a) mean water level η inside the bay and (b) residual EFV in the bay computed without (black line) and with (colored lines and symbols) wave forcing under different incident wave conditions.

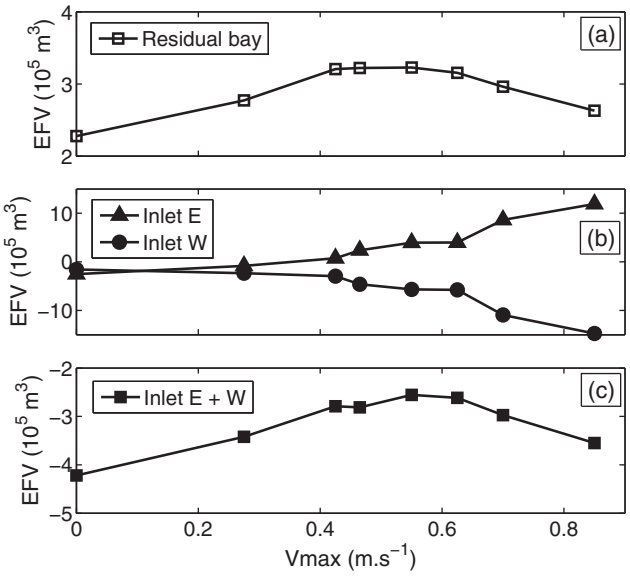

Figure 13. (a) Residual EFV in the bay at the end of the simulation (day 2), (b) total EFV exchange through the eastern inlet (triangles) and through the western inlet (circles), and (c) total EFV exchange through both inlets over the simulated time interval (day 0–2), as a function of the maximum velocity $V_{\max}$ of the longshore current.

[41] On the contrary, a further increase in incident wave energy promotes a larger bay flushing, as illustrated by Figure 13a for $V_{\max} > 0.6$ m s^{-1}. Figures 13b and 13c show that for these larger $V_{\max}$ values, the increase in the freshwater outflow through the western inlet becomes more important than the outflow reduction in the eastern inlet. Indeed, the location of the surf zone and the very strong longshore current in the rocky area result in an even more important westward advection of freshwater masses inside the bay. Freshwater finally concentrates in the western part of the bay, close to the western bay inlet. This enables a higher freshwater outflow through the western inlet during the tide cycle, which results in a reduction of the retention effect of wave forcing.

[42] Model results thus suggest a major sensitivity of the bay flushing to the incident wave energy and the corresponding longshore current velocity. For typical incident peak period $T_p = 10$ s and peak direction $\theta_p = 310°$, maximum freshwater retention in the bay is found for H_s between 1 and 2 m, which corresponds to $V_{\max}$ values between 0.5 and 0.6 m s^{-1}. This corresponds also to the range of wave conditions encountered during the episode from 22 to 28 September 2010, examined in this paper.

5. Conclusions

[43] A 3-D wave-current numerical model was used to investigate the effect of tides, winds, and waves on the dynamics of a small estuarine bay. In the studied configuration, a strong salinity stratification is associated with river plumes, leading to a highly 3-D behavior. To account for this feature, the flow model resolves the vertical structure of wave momentum and forcing, as well as wave-induced vertical mixing. Although additional efforts will be required for a quantitative small-scale validation of modeled flow patterns, the present work takes advantages of the 3-D model representation to propose an analysis of local dispersion processes, as a first step in the study of the complex bay dynamics.

[44] A time interval, combining both a river flood event and an increase in incident wave energy, was examined to illustrate possible effects of waves on the bay response to freshwater inputs. Results of numerical modeling suggest a significant impact of waves on the bay dynamics, larger than wind effect during the examined time interval. Obliquely incident waves refract and break over a rocky platform inside the bay, resulting in a longshore current strongly modulated by tide. During the examined energetic wave event ($H_s \sim 2$ m), the computed current intensity is very large in the surf zone area, compared to the slower circulation in the other deeper parts of the bay.

[45] Modeled salinity fields show a thin surface layer with lower salinity, associated with river plumes spreading inside the bay. The surface layer depth and profile shape exhibit a large space-time variability along the tide cycle, related to transport and mixing inside the bay. During the examined high-energy wave episode, model results suggest that the wave-induced longshore current reduces freshwater outflow through the bay inlets. The asymmetric wave forcing on the circulation results in a higher concentration of freshwater from the main river in the southeastern part of the bay. The model is further used to determine the related effects on the local freshwater balance of the bay at the scale of the river flood event. It is found that waves can contribute to concentrate freshwater inside the bay. At the end of the examined event, the estimated freshwater volume inside the bay is 40% higher and the freshwater outflow is still reduced by a factor 5 due to waves.

[46] The sensitivity of the wave-induced freshwater retention to incident wave conditions was finally investigated. The analysis of model results shows a strong dependence of the bay flushing to incident wave energy and to the corresponding longshore current velocity. Maximum freshwater volume inside the bay was found for intermediate offshore wave heights 1 m $< H_s <$ 2 m and longshore current velocity $V_{\max} \sim 0.6$ m s^{-1}, whereas freshwater retention may be reduced by a factor 2 for lower ($H_s \sim 0.5$ m, $V_{\max} \sim 0.25$ m s^{-1}) or higher ($H_s \sim 4$ m, $V_{\max} \sim 0.8$ m s^{-1}) incident wave energy.

[47] The wave-induced reduction of the bay flushing suggested by this modeling study may have a large impact on the exchanges between the bay and the inner shelf. In particular, it may be a key mechanism in the dispersion of terrestrial contaminant carried by rivers in the near shore, contributing to determine water quality inside the bay.

Appendix A: MOHID-GLM Implementation

[48] This appendix presents the 3-D wave-current set of equations implemented in MOHID-GLM. The formulation corresponds to *Ardhuin et al*. [2008b] as adapted by *Bennis et al*. [2011], with some specificities related to the MOHID model and to the studied area. A synopsis of MOHID-GLM is given below. The reader is referred to *Delpey* [2012] for a detailed description of the code implementation.

A1. Governing Equations

[49] The quasi-Eulerian velocity field, noted $\hat{\mathbf{u}}=(\hat{u}_1,\hat{u}_2,\hat{w})$, is defined as [*Jenkins*, 1989]

$$(\hat{u}_1,\hat{u}_2,\hat{w})=(\overline{u}_1^L,\overline{u}_2^L,\overline{w}^L)-(u_1^S,u_2^S,w^S), \tag{A1}$$

where $\overline{\mathbf{u}}^{\mathbf{L}}=(\overline{u}_1^L,\overline{u}_2^L,\overline{w}^L)$ is the Lagrangian mean velocity field and $\mathbf{u}^{\mathbf{S}}=(u_1^S,u_2^S,w^S)$ is the Stokes drift velocity field.

[50] The vertical coordinate change used by *Ardhuin et al*. [2008b] corrects the vertical coordinate for the GLM-induced vertical displacement, so that $\hat{\mathbf{u}}$ and $\overline{\mathbf{u}}^{\mathbf{L}}$ are nondivergent. The nondivergence of $\overline{\mathbf{u}}^{\mathbf{L}}$ is used by the model in its vertically integrated form, from the bottom depth h to the mean surface elevation $\hat{\eta}$, which results in the following equation for $\hat{\eta}$:

$$\frac{\partial\hat{\eta}}{\partial t}+\frac{\partial\left(\langle\hat{u}_\alpha\rangle+\langle u_\alpha^S\rangle\right)}{\partial x_\alpha}=0, \tag{A2}$$

where t is the time; $\{x_\alpha,\alpha\in[1,2]\}$ are the horizontal space coordinates; z is the vertical coordinate; $\langle(.)\rangle$ denotes depth-integrated variables; and the summation convention for repeated indices is used. It should be noted that the vertical coordinate change used by *Ardhuin et al*. [2008b] corrects the quasi-Eulerian free surface position $z=\hat{\eta}$ for the Stokes correction of η, so that it is equal to the local phase-averaged free surface position $z=\overline{\eta}$.

[51] The conservation equation implemented in MOHID-GLM for the quasi-Eulerian momentum is given in a flux-divergence form by

$$\begin{aligned}\frac{\partial\hat{u}_\alpha}{\partial t}+\frac{\partial\left[(\hat{u}_\beta+u_\beta^S)\hat{u}_\alpha\right]}{\partial x_\beta}+\frac{\partial\left[(\hat{w}+w^S)\hat{u}_\alpha\right]}{\partial z}\\ =-\frac{1}{\rho_0}\frac{\partial\overline{p}^H}{\partial x_\beta}-\frac{\partial S^J}{\partial x_\beta}+u_\beta^S\frac{\partial\hat{u}_\beta}{\partial x_\alpha}\\ +\frac{\partial}{\partial x_\beta}\left(K_H\frac{\partial\hat{u}_\alpha}{\partial x_\beta}\right)+\frac{\partial}{\partial z}\left(K_V\frac{\partial\hat{u}_\alpha}{\partial z}\right),\end{aligned} \tag{A3}$$

where ρ_0 is the water mean density; $\overline{p}^H$ denotes the mean pressure, which is assumed to be hydrostatic; S^J is the wave-induced pressure term; K_H, K_V are the horizontal and vertical eddy viscosities, respectively. This equation is equivalent to equations (12) and (13) in *Bennis et al*. [2011] because $\mathbf{u}^{\mathbf{S}}$ is nondivergent [*Ardhuin et al*., 2008b]. Here the momentum equation is implemented using the Cartesian z-coordinate, as the numerical resolution is always achieved by MOHID in the Cartesian space for any type of vertical discretization (Cartesian or not), with a procedure equivalent to a generic vertical coordinate [see *Martins et al*., 2001]. In the present study, a sigma vertical discretization is used (terrain-following).

[52] In equations (A2) and (A3), the wave related terms S^J and u_α^S are given, respectively, by

$$S^J=\int_{\mathbf{k}}gk\frac{E(\mathbf{k})}{\sinh 2kD}\mathrm{d}\mathbf{k}, \tag{A4}$$

and

$$u_\alpha^S=\int_{\mathbf{k}}U_\alpha^{SS}(\mathbf{k})\frac{\cosh(2kz+2kh)}{\sinh^2(kD)}\mathrm{d}\mathbf{k}\quad\text{if}\quad kD<6, \tag{A5}$$

$$u_\alpha^S=\int_{\mathbf{k}}U_\alpha^{SS}(\mathbf{k})\exp[2k(z-\eta)]\mathrm{d}\mathbf{k}\quad\text{if}\quad kD\geq 6, \tag{A6}$$

where $k=||\mathbf{k}||$; σ is the wave intrinsic pulsation; and $U_\alpha^{SS}(\mathbf{k})=\sigma k_\alpha E(\mathbf{k})$ denotes the spectrum of the surface Stokes drift horizontal components. The vertical component of the Stokes drift w^S can be computed using the nondivergence of the Stokes drift velocity field by

$$w^S(z)=-u_\alpha^S(-h)\frac{\partial h}{\partial x_\alpha}-\int_{-h}^{z}\frac{\partial u_\alpha^S}{\partial x_\alpha}(z')\,\mathrm{d}z'. \tag{A7}$$

[53] Density evolution is computed from S and T through a state relationship [*UNESCO*, 1981]. If C denotes S or T, the conservation of C is expressed by

$$\begin{aligned}\frac{\partial C}{\partial t}+\frac{\partial\left[(\hat{u}_\alpha+u_\alpha^S)C\right]}{\partial x_\alpha}+\frac{\partial\left[(\hat{w}+w^S)C\right]}{\partial z}\\ =\frac{\partial}{\partial x_\alpha}\left(K_H\frac{\partial C}{\partial x_\alpha}\right)+\frac{\partial}{\partial z}\left(K_C\frac{\partial C}{\partial z}\right)+S_C,\end{aligned} \tag{A8}$$

where K_C and S_C are the vertical eddy diffusivity and the source term associated with the tracer C, respectively. In equation (A8), the horizontal eddy diffusivity for C is equal to the horizontal eddy viscosity, both noted K_H.

A2. Boundary Conditions for the Quasi-Eulerian Flow

[54] Boundary conditions in MOHID-GLM allow to account for different effects of waves on the quasi-Eulerian flow. Kinematic surface and bottom boundary conditions are, respectively, given by

$$\frac{\partial\hat{\eta}}{\partial t}+\left(\hat{u}_\alpha+u_\alpha^S\right)\frac{\partial\hat{\eta}}{\partial x_\alpha}=\hat{w}+w^S\ \text{at}\ z=\hat{\eta}(x_1,x_2,t), \tag{A9}$$

$$\left(\hat{u}_\alpha+u_\alpha^S\right)\frac{\partial(-h)}{\partial x_\alpha}=\hat{w}+w^S\ \text{at}\ z=-h(x_1,x_2). \tag{A10}$$

[55] Fluxes of momentum from wind and from wave breaking are introduced in the equations through the dynamic surface boundary condition:

$$K_V\frac{\partial\hat{u}_\alpha}{\partial z}=\tau_\alpha^a-\tau_\alpha^{aw}+\tau_\alpha^{oc}\ \text{at}\ z=\hat{\eta}(x_1,x_2,t), \tag{A11}$$

where $\tau^{\mathbf{a}}$ is the total momentum flux from the atmosphere to the ocean (wind stress), computed from the local wind speed using a quadratic friction law, as proposed by *Large and Pond* [1981]; $\tau^{\mathbf{aw}}$ is the momentum flux from the atmosphere to waves (or wave-supported wind stress); and $\tau^{\mathbf{oc}}$ is the momentum flux from waves to the mean current due to wave breaking. $\tau^{\mathbf{aw}}$ and $\tau^{\mathbf{wo}}$ are computed from spectral wave energy source terms S_{in} and S_{oc}, respectively (introduced in paragraph 3.2.), according to *Ardhuin et al*. [2009, 2010].

[56] At the bottom, the combined wave and current stress $\tau^{\mathbf{b}}$ is computed according to *Soulsby et al*. [1995]. It results in the following condition:

$$K_V \frac{\partial \hat{u}_\alpha}{\partial z} = \tau^b_{c,\alpha}\left[1+1.2\left(\frac{||\tau^{\mathbf{b}}_{\mathbf{w}}||}{||\tau^{\mathbf{b}}_{\mathbf{c}}||+||\tau^{\mathbf{b}}_{\mathbf{w}}||}\right)^{3.2}\right] \quad \text{at } z=-h(x_1,x_2), \tag{A12}$$

where the mean-current bottom stress $\tau^{\mathbf{b}}_{\mathbf{c}}$ and the wave-induced bottom stress $\tau^{\mathbf{b}}_{\mathbf{w}}$ are given, respectively, by

$$\tau^{\mathbf{b}}_{\mathbf{c}} = \rho_0 C_D ||\hat{\mathbf{u}}||\hat{\mathbf{u}} \quad \text{and} \quad \tau^{\mathbf{b}}_{\mathbf{w}} = \frac{1}{2}\rho_0 F_w ||\mathbf{u}'||\mathbf{u}', \tag{A13}$$

with C_D a *Chezy*-type bottom drag coefficient; F_w a bottom friction coefficient; and $\mathbf{u}'$ the wave orbital velocity. In (A13) both $\hat{\mathbf{u}}$ and $\mathbf{u}'$ are evaluated at the top of the bottom boundary layer (which is not resolved here). The bottom drag coefficient C_D is given from a bottom roughness length $z_{0,b}$ by

$$C_D = \left(\frac{\kappa}{\log\left(\frac{z'+z_{0,b}}{z_{0,b}}\right)}\right)^2, \tag{A14}$$

where z' is the distance from the top of the bottom boundary layer. In accordance with *Soulsby et al*. [1995], the friction coefficient F_w is evaluated by

$$F_w = 1.39\left(\frac{||\mathbf{u}'||}{\sigma_p z_{0,b}}\right)^{-0.52}, \tag{A15}$$

where $\sigma_p = 2\pi f_p$, with f_p the peak frequency.

[57] At open boundaries, a mixed radiation-relaxation condition is used, transferring the methodology proposed by *Marchesiello et al*. [2001] to the present smaller scale application. A Flather radiation condition is applied for the barotropic flow [*Flather*, 1976]. The original formulation is modified to account now for the linearized barotropic equilibrium of the quasi-Eulerian flow, instead of the total flow. It results in the following condition at open boundaries:

$$\hat{\eta}-\hat{\eta}_{\text{ext}} = \pm\sqrt{\frac{D}{g}}\left[\left(\langle\hat{\mathbf{u}}\rangle+\langle\mathbf{u}^{\mathbf{S}}\rangle\right)\cdot\mathbf{n}-\left(\langle\hat{\mathbf{u}}_{\text{ext}}\rangle+\langle\mathbf{u}^{\mathbf{S}}{}_{\text{ext}}\rangle\right)\cdot\mathbf{n}\right], \tag{A16}$$

where $\hat{\eta}_{\text{ext}}, \hat{\mathbf{u}}_{\text{ext}}, \mathbf{u}^{\mathbf{S}}{}_{\text{ext}}$ are the imposed values of $\hat{\eta}, \hat{\mathbf{u}}, \mathbf{u}^{\mathbf{S}}$ at the open boundary; $\mathbf{n}$ is the vector normal to the open boundary. In addition, a relaxation scheme is used for the baroclinic flow. If ϕ denotes the horizontal components of the baroclinic velocity, the open boundary condition is given by

$$\frac{\partial\phi}{\partial t} = -\frac{1}{\tau_{\text{relax}}}(\phi-\phi_{\text{ext}}), \tag{A17}$$

where τ_{relax} is a relaxation coefficient, which is set a to low value in a nudging layer near the boundary and to a very large value in the rest of the domain. Baroclinic modes are not radiated at open boundaries, following arguments presented, for example, by *Blayo and Debreu* [2005] and *Leitão et al*. [2008]. A similar relaxation scheme is applied to salinity and temperature fields.

[58] At land boundaries, a free slip condition is assumed with zero depth-integrated total mass flux in direction normal to the boundary.

A3. Turbulent Closure

[59] In equations (A3) and (A8), a constant value is used for the horizontal eddy viscosity K_H. This simple parameterization is used here as a first approximation, and the main features described in this paper were still obtained when testing different values of K_H (not shown). However, the refinement of this parameterization, e.g., to account for horizontal diffusion due to wave breaking in the surf zone [e.g., *Feddersen*, 2007; *Spydell et al*., 2007, 2009], would be an interesting aspect to be investigated as part of further work.

[60] For the vertical turbulent closure, the MOHID system is coupled to the General Ocean Turbulence Model (GOTM) [*Burchard and Bolding*, 2001], a 1-D water column model proposing several turbulent closure schemes. In the present study, a $\mathcal{K}-\epsilon$ model [*Rodi*, 1980] is used. The vertical eddy viscosity and diffusivity (K_V, K_C) are parameterized as $(K_V, K_C) = (S_V, S_C)(q^2/2)^2\epsilon^{-1}$, where $q^2/2$ is the TKE, ϵ is the TKE-dissipation rate, and S_V, S_C are stability functions. The formulation proposed by *Canuto et al*. [2001] is used for S_V and S_C. Equations for $q^2/2$ and ϵ are given by

$$\frac{\partial(q^2/2)}{\partial t} = \frac{\partial}{\partial z}\left(K_V\frac{\partial(q^2/2)}{\partial z}\right)+P_s+P_b-\epsilon, \tag{A18}$$

$$\frac{\partial\epsilon}{\partial t} = \frac{\partial}{\partial z}\left(\frac{K_V}{\sigma_\epsilon}\frac{\partial\epsilon}{\partial z}\right)+\frac{2\epsilon}{q^2}(c_1P_s+c_3P_b-c_2\epsilon), \tag{A19}$$

with P_s and P_b the TKE productions by vertical shear and buoyancy, respectively, given by $P_s = \frac{\partial u_x}{\partial z}\frac{\partial u_x}{\partial z}$ and $P_b = -\frac{g}{\rho_0}\frac{\partial\rho}{\partial z}$; σ_ϵ is the Schmidt number for ϵ; and c_1, c_2, c_3 are empirical constants, which are prescribed according to *Canuto et al*. [2001] for this study.

[61] Wave breaking can greatly affect vertical mixing as it provides an important source of TKE near the surface compared to P_s or P_b [*Agrawal et al*., 1992; *Terray et al*., 1996; *Feddersen*, 2012a, 2012b]. Effects of wave breaking on vertical turbulence are taken into account through the surface boundary conditions for (A18) and (A19), which were adapted from *Craig and Banner* [1994], *Craig* [1996] by *Burchard* [2001]. The surface boundary conditions for $q^2/2$ and ϵ are, respectively, given by

$$K_V\frac{\partial(q^2/2)}{\partial z} = F_{oc}, \tag{A20}$$

$$\frac{K_V}{\sigma_\epsilon}\frac{\partial\epsilon}{\partial z} = \frac{K_V}{\sigma_\epsilon}C_0^3\left(\frac{3}{2}\frac{C_0^3}{S_V}F_{oc}+\kappa(q^2/2)^{\frac{3}{2}}\right)\frac{1}{\kappa^2(z'+z_{0,s})^2}, \tag{A21}$$

with F_{oc} the surface TKE flux due to wave breaking; C_0^3 a constant; z' the vertical distance from the surface; and $z_{0,s}$ a surface roughness length. In addition to these boundary conditions, *Burchard* [2001] established a parameterization of the Schmidt number σ_ϵ as a linear function of $(P_s+P_b)/\epsilon$ in order to obtain a behavior of the mixing length $l = C_0^3(q^2/2)^{\frac{3}{2}}\epsilon^{-1}$ like $l = \kappa(z'+z_{0,s})$ near the surface, as prescribed by *Craig and Banner* [1994]. In the present work, F_{oc} is specified from the wave breaking dissipation term S_{oc},

computed by the wave model according to *Janssen et al*. [2004]. Wave breaking also envolves an enhanced value of $z_{0,s}$ [*Craig and Banner*, 1994], which is proportional to the total significant wave height H_S in the present application [*Terray et al*., 1996, 2000]:

$$z_{0,s} = \alpha_0 H_S, \tag{A22}$$

with α_0 a constant. The studied bay shows areas exposed to incident waves and areas sheltered by breakwaters. The main exposed area corresponds to the surf zone in the northeast of the bay, where the whole wave spectrum (including swell) can be affected by depth-induced breaking. The rest of the domain is mostly sheltered by the breakwaters, so that the sea state generally consists in a small wind sea which is generated locally. The total H_S should thus be representative of the wave spectrum part which is affected by breaking in both exposed (depth-induced breaking) and sheltered (whitecapping) areas. As a consequence, $z_{0,s}$ is considered proportional to the total H_S, because it generally provides the scale of breaking waves in the studied bay.

[62] In the present work, wave related terms H_S, f_p, S^J, U^{SS}, τ^{aw}, τ^{oc}, and F_{oc} are computed by WWIII from the wave field and source terms, and then transmitted to MOHID-GLM for the flow computation.

Appendix B: Discussion of Wave Model Results and Parameterization

[63] To obtain a better agreement with field data, the friction coefficient in the bay has been significantly increased compared to more common values used over sand beds [e.g., *Hasselmann et al*., 1973]. Because of the present site complexity involving combined refraction, wave breaking and frictional dissipation, it is difficult to confirm the role of bottom friction in the observed wave transformation. However, preliminary tests with a constant Nikuradse roughness length of 10 cm give similar results. This value is comparable to the 12 cm used for rock platforms by *Ardhuin and Roland* [2013]. Such a high friction level could be related to the unusually rough surface of the rocky platform (Figure 2) and of other rocky formations over the inner shelf offshore of the bay [*Augris et al*., 1999]. The importance of wave frictional dissipation has been emphasized by several authors in shallow areas with very rough bottoms, in particular coral reefs [e.g., *Lowe et al*., 2005; *Cialone and Mckee Smith*, 2007; *Filipot and Cheung*, 2012]. For example, based on field measurements on the reef flat of Kaneohe Bay, Hawaii, *Lowe et al*. [2005] calculated the averaged value of the wave friction factor $f_w = 0.28 \pm 0.04$, and mentioned that this value is 30 times larger than the typical value of 0.01 for flat sandy bottoms. According to the model of *Madsen et al*. [1988], f_w can be related to Γ by

$$\Gamma = f_w \frac{g}{\sqrt{2}} U_{\mathrm{rms}}, \tag{B1}$$

where U_{rms} is the root-mean-square wave orbital velocity at the bottom. For typical values of U_{rms} between 0.1 and 0.5 m s^{-1}, this leads to Γ values between 0.2 and 1.0 m^2 s^{-3}.

Table B1. Errors Between Observed and Simulated Wave Bulk Parameters at Anglet Buoy, AWAC, ADVN and ADVS Locations From 22 to 28 September[a]

		Model With Default Γ	Model With Selected Γ
Sensor	Parameter	*RMSE, NRMSE*	*RMSE, NRMSE*
Anglet Buoy	H_S	13 cm, 7%	13 cm, 7%
	T_{02}	0.6 s, 8%	0.6 s, 8%
	D_m	3°	3°
AWAC	H_S	20 cm, 16%	16 cm, 13%
	T_{02}	1.5 s, 25%	1.3 s, 21%
	D_m	4°	4°
ADVN	H_S	36 cm, 65%	17 cm, 31%
	T_{02}	2.3 s, 37%	1.8 s, 31%
	D_m	8°	8°
ADVS	H_S	19 cm, 50%	7 cm, 19%
	T_{02}	2.4 s, 34%	2.0 s, 32%
	D_m	7°	7°

[a]Error statistics at the ADVS location are given for the shorter time interval from 25 to 27 September (due to the sensor dysfunction).

This range of Γ values also corresponds to the order of magnitude obtained for another Hawaiian reef area by *Cialone and Mckee Smith* [2007], who used a coefficient $c_f = \Gamma/g$ between 0.05 and 0.12 m s^{-1}. However, specific investigations would be required to confirm that the level of frictional wave dissipation over the studied rocky area can be comparable to that induced by coral reefs. This large Γ value may be necessary here to correct for all possible errors in the definition of the offshore boundary conditions.

[64] Figures 5 and 6 show that the increase in Γ significantly improves model results, in particular inside the bay at the ADVN and ADVS locations. Table B1 gives root-mean-square errors (RMSE) between observed and modeled wave height H_s, mean period T_{02} and mean direction D_m for both default and selected model parameterization. Normalized root-mean-square errors (NRMSE) are also given for H_s and T_{02}. The two error indicators are defined, respectively, as

$$RMSE = \left[\frac{1}{N}\sum_{i=1}^{N}(S_i - O_i)^2\right]^{1/2}, \; NRMSE = \frac{RMSE}{RMS}, \tag{B2}$$

where $(O_i)_{i=1..N}$ and $(S_i)_{i=1..N}$ are the observed and simulated values, respectively, and RMS denotes the root-mean-square of $(O_i)_{i=1..N}$. Error statistics are given for the three sensors deployed in the bay and also for the Anglet wave buoy, located in the northeast of domain G1 at depth 50 m (Figure 4).

[65] Results obtained with selected parameters compare reasonably with field data during the 6 days interval examined here, for both low and high-energy conditions. Wave energy associated with the long swell is still overestimated by the model during the high-energy episode (Figure 6b), possibly due to local nonresolved bathymetric effects outside the bay. The computed wave transformation in the east part of the bay reproduces the direction shift and wave dissipation due to the rocky platform and the related tidal modulation. The higher error level at the ADVN location could be related to the horizontal resolution of the

computational grid, which limits the representation of wave refraction over the complex bathymetry of the bay. Indeed, calculations carried out with a spectral refraction-diffraction model generally produced larger spatial gradients (not shown), while giving the same patterns of wave heights at scales of 100 m and larger inside the bay. The use of a constant breaking parameter γ may also be a limitation [e.g., *Bruneau et al*., 2011].

[66] **Acknowledgments.** M.T.D. acknowledges the support of a research grant from ANRT (CIFRE grant), and F.A. is supported by IOWAGA and Field_AC projects. The present study was supported in part by the LOREA project, led by the Conseil Général des Pyrénées Atlantiques (http://www.lorea.eu/). LOREA 2010 field experiment was performed in collaboration with AZTI-Tecnalia (Marine Research Division), G.E.O Transfert and CASAGEC. Lagrangian drifter experiment was performed in collaboration with the SHOM.

References

Abadie, S., R. Butel, H. Dupuis, and C. Briere (2005), Paramètres statistiques de la houle au large de la côte sud-aquitaine, *Comptes Rendus Geosci.*, *337*(8), 769–776.

Agrawal, Y. C., E. A. Terray, M. A. Donelan, P. A. Hwang, A. J. Williams, W. Drennan, K. Kahma, and S. Kitaigorodskii (1992), Enhanced dissipation of kinetic energy beneath breaking waves, *Nature*, *359*, 219–220.

Ahn, J. H., S. B. Grant, C. Q. Surbeck, P. M. DiGiacomo, N. P. Nezlin, and S. Jiang (2005), Coastal water quality impact of stormwater runoff from an urban watershed in southern California, *Environ. Sci. Technol.*, *39*(16), 5940–5953.

Aiki, H., and R. J. Greatbatch (2012), The vertical structure of the surface wave radiation stress for circulation over a sloping bottom as given by thickness-weighted-mean theory, *J. Phys. Oceanogr.*, *42*, 725–747, doi: 10.1175/JPO-D-12-059.1.

Andrews, D. G., and M. E. McIntyre (1978), An exact theory of nonlinear waves on a Lagrangian-mean flow, *J. Fluid Mech.*, *89*, 609–646.

Ardhuin, F., and A. Roland (2013), The development of spectral wave models: Coastal and coupled aspects, in *Proceedings of Coastal Dynamics 2013: 7th International Conference on Coastal Dynamics*, pp. 25–38, University of Bordeaux, Bordeaux, France.

Ardhuin, F., A. D. Jenkins, and K. A. Belibassakis (2008a), Comments on the three-dimensional current and surface wave equations, *J. Phys. Oceanogr.*, *38*(6), 1340–1350.

Ardhuin, F., N. Rascle, and K. Belibassakis (2008b), Explicit wave-averaged primitive equations using a generalized Lagrangian mean, *Ocean Modell.*, *20*(1), 35–60, doi:10.1016/j.ocemod.2007.07.001.

Ardhuin, F., L. Marié, N. Rascle, P. Forget, and A. Roland (2009), Observation and estimation of Lagrangian, stokes, and Eulerian currents induced by wind and waves at the sea surface, *J. Phys. Oceanogr.*, *39*(11), 2820–2838, doi:10.1175/2009JPO4169.1.

Ardhuin, F., et al. (2010), Semi-empirical dissipation source functions for wind-wave models: Part I: Definition, calibration and validation at global scales, *J. Phys. Oceanogr.*, *40*(9), 1917–1941, doi:10.1175/2010JPO4324.1.

Ardhuin, F., A. Roland, F. Dumas, A.-C. Bennis, A. Sentchev, P. Forget, J. Wolf, F. Girard, P. Osuna, and M. Benoit (2012), Numerical wave modeling in conditions with strong currents: Dissipation, refraction and relative wind, *J. Phys. Oceanogr.*, *42*, 2101–2120.

Augris, C., P. Cirac, C. Satra, and J.-P. Mazé (1999), *Le domaine marin côtier du Pays Basque. Carte des formations superficielles et carte morpho-bathymétrique. Echelle 1/20 000*, IFREMER, Conseil Général des Pyrénées Atlantiques-Communauté Européenne, Brest, France.

Battjes, J. A., and J. P. F. M. Janssen (1978), Energy loss and set-up due to breaking of random waves, in *Proceedings of the 16th International Conference on Coastal Engineering*, pp. 569–587, ASCE Press, Reston, Va.

Bennis, A. C., F. Ardhuin, and F. Dumas (2011), On the coupling of wave and three-dimensional circulation models: Choice of theoretical framework, practical implementation and adiabatic tests, *Ocean Modell.*, *40*, 260–272, doi:10.1016/j.ocemod.2011.09.003.

Bidlot, J. R., S. Abdalla, and P. A. E. M. Janssen (2005), A revised formulation for ocean wave dissipation in cy25r1, *Tech. Rep. Memo. R60.9/JB/0516, Res. Dep*., European Centre for Medium-Range Weather Forecasts (ECMWF), Reading, U. K.

Blayo, E., and L. Debreu (2005), Revisiting open boundary conditions from the point of view of characteristic variables, *Ocean Modell.*, *9*(3), 231–252.

Boehm, A. B., S. B. Grant, J. H. Kim, S. L. Mowbray, C. D. McGee, C. D. Clark, D. M. Foley, and D. E. Wellman (2002), Decadal and shorter period variability of surf zone water quality at Huntington Beach, California, *Environ. Sci. Technol.*, *36*(18), 3885–3892.

Boehm, A. B., D. P. Keymer, and G. G. Shellenbarger (2005), An analytical model of enterococci inactivation, grazing, and transport in the surf zone of a marine beach, *Water Res.*, *39*(15), 3565–3578.

Braunschweig, F., P. C. Leitao, L. Fernandes, P. Pina, and R. J. J. Neves (2004), The object oriented design of the integrated water modelling system MOHID, in *Proceedings of the XVth International Conference on Computational Methods in Water Ressources*, pp. 1–12, Elsevier, Oxford, U. K.

Bruneau, N., P. Bonneton, B. Castelle, and R. Pedreros (2011), Modeling rip current circulations and vorticity in a high-energy mesotidal-macrotidal environment, *J. Geophys. Res*., *116*, C07026, doi:10.1029/2010JC006693.

Burchard, H. (2001), Simulating the wave-enhanced layer under breaking surface waves with two-equation turbulence models, *J. Phys. Oceanogr.*, *31*(11), 3133–3145.

Burchard, H., and K. Bolding (2001), Comparative analysis of four second-moment turbulence closure models for the oceanic mixed layer, *J. Phys. Oceanogr.*, *31*(8), 1943–1968.

Canuto, V. M., A. Howard, Y. Cheng, and M. S. Dubovikov (2001), Ocean turbulence. Part I: One-point closure model momentum and heat vertical diffusivities, *J. Phys. Oceanogr.*, *31*(6), 1413–1426.

Cialone, M. A., and J. Mckee Smith (2007), Wave transformation modeling with bottom friction applied to southern Oahu reefs, in *10th International Workshop on Wave Hindcasting and Forecasting & Coastal Hazard Assessment,* pp. 1–12, North Shore, Oahu, Hawaii.

Coelho, H., R. Neves, M. White, P. C. Leitão, and A. J. Santos (2002), A model for ocean circulation on the Iberian coast, *J. Mar. Syst.*, *32*, 153–179.

Craig, P. D. (1996), Velocity profiles and surface roughness under breaking waves, *J. Geophys. Res.*, *101*, 1265–1277.

Craig, P. D., and M. L. Banner (1994), Modeling wave-enhanced turbulence in the ocean surface layer, *J. Phys. Oceanogr.*, *24*(12), 2546–2559.

Delpey, M. T. (2012), Étude de la dispersion en zone littorale sous l'effet de la circulation tridimensionnelle forcée par les vagues. Application à la Baie de Saint Jean de Luz-Ciboure et au littoral de Guéthary-Bidart, PhD thesis, Univ. de Bretagne Occident., Brest, France.

Feddersen, F. (2007), Breaking wave induced cross-shore tracer dispersion in the surfzone: Model results and scalings, *J. Geophys. Res.*, *112*, C09012, doi:10.1029/2006JC004006.

Feddersen, F. (2012a), Observations of the surf-zone turbulent dissipation rate, *J. Phys. Oceanogr.*, *42*, 386–399.

Feddersen, F. (2012b), Scaling surfzone turbulence, *Geophys. Res. Lett.*, *39*, L18613, doi:10.1029/2012GL052970.

Fiandrino, A., Y. Martin, P. Got, J. L. Bonnefont, and M. Troussellier (2003), Bacterial contamination of Mediterranean coastal seawater as affected by riverine inputs: Simulation approach applied to a shellfish breeding area (Thau lagoon, France), *Water Res.*, *37*(8), 1711–1722.

Filipot, J. F., and F. Ardhuin (2012), A unified spectral parameterization for wave breaking: From the deep ocean to the surf zone, *J. Geophys. Res.*, *117*, C00J08, doi:10.1029/2011JC007784.

Filipot, J. F., and K. F. Cheung (2012), Spectral wave modeling in fringing reef environments, *Coastal Eng.*, *67*, 67–79, doi:10.1016/j.coastaleng.2012.04.005.

Flather, R. A. (1976), A tidal model of the northwest European continental shelf, *Mém. Soc. R. Sci. Liège*, *10*(6), 141–164.

Garrett, C. (1976), Generation of Langmuir circulations by surface waves: A feedback mechanism, *J. Mar. Res.*, *34*, 117–130.

Given, S., L. H. Pendleton, and A. B. Boehm (2006), Regional public health cost estimates of contaminated coastal waters: A case study of gastroenteritis at southern California beaches, *Environ. Sci. Technol.*, *40*(16), 4851–4858.

Grant, S. B., J. H. Kim, B. H. Jones, S. A. Jenkins, J. Wasyl, and C. Cudaback (2005), Surf zone entrainment, along-shore transport, and human health implications of pollution from tidal outlets, *J. Geophys. Res.*, *110*, C10025, doi:10.1029/2004JC002401.

Groeneweg, J. (1999), Wave-current interactions in a generalized Lagrangian mean formulation, PhD thesis, Delft Univ. of Technol., Delft, Netherlands.

Haas, K., and J. Warner (2009), Comparing a quasi-3D to a full 3D nearshore circulation model: SHORECIRC and ROMS, *Ocean Modell.*, *26*(1–2), 91–103.

Haas, K. A., and I. A. Svendsen (2002), Laboratory measurements of the vertical structure of rip currents, *J. Geophys. Res.*, *107*(C5), 2047, doi: 10.1029/2001JC000911.

Hasselmann, K., et al. (1973), Measurements of wind-wave growth and swell decay during the joint north sea wave project (jonswap), *Ergänzungsheft zur Dtsch. Hydrogr. Z. Reihe*, *8*(12), 95.

Hasselmann, S., K. Hasselmann, J. H. Allender, and T. P. Barnett (1985), Computation and parameterizations of the nonlinear energy transfer in a gravity-wave spectrum. Part II: Parameterizations of the nonlinear energy transfer for application in wave models, *J. Phys. Oceanogr.*, *15*, 1378–1391.

Janssen, P. A. E. M., O. Saetra, C. Wettre, and H. Hersbach (2004), Impact of the sea state on the atmosphere and ocean, *Ann. Hydrogr.*, *3*(772), 3–1–3–23.

Jenkins, A. (1989), The use of a wave prediction model for driving a near-surface current model, *Dtsch. Hydrogr. Z.*, *42*(3), 133–149.

Lane, E. M., J. M. Restrepo, and J. C. McWilliams (2007), Wave-current interaction: A comparison of radiation-stress and vortex-force representations, *J. Phys. Oceanogr.*, *37*, 1122–1141.

Large, W. G., and S. Pond (1981), Open ocean momentum flux measurements in moderate to strong winds, *J. Phys. Oceanogr.*, *11*(3), 324–336.

Leitão, P., H. Coelho, A. Santos, and R. Neves (2005), Modelling the main features of the Algarve coastal circulation during July 2004: A downscaling approach, *J. Atmos. Ocean Sci.*, *10*, 421–462.

Leitão, P. C., G. Riflet, L. Fernandes, R. Fernandes, and A. Canas (2008), Towards an hydrodynamic an biogeochemical operational model of the Portuguese coast, in *Proceedings of International Conference on Mathematics and Continuum Mechanics 2008*, Centro Internacional de Matematica (International Center for Mathematics), Coimbra, Portugal.

Lentz, S. J., M. Fewings, P. Howd, J. Fredericks, and K. Hathaway (2008), Observations and a model of undertow over the inner continental shelf, *J. Phys. Oceanogr.*, *38*, 2341–2357, doi:10.1175/2008JPO3986.1.

Longuet-Higgins, M. S. (1970a), Longshore currents generated by obliquely incident sea waves: 1, *J. Geophys. Res.*, *75*, 6778–6789.

Longuet-Higgins, M. S. (1970b), Longshore currents generated by obliquely incident sea waves: 2, *J. Geophys. Res.*, *75*, 6790–6801.

Longuet-Higgins, M. S., and R. W. Stewart (1962), Radiation stress and mass transport in gravity waves, with application to surf beats, *J. Fluid Mech.*, *13*(04), 481–504.

Longuet-Higgins, M. S., and R. W. Stewart (1964), Radiation stresses in water waves: A physical discussion with applications, *Deep Sea Res. Oceanogr. Abstr.*, *11*, 529–562.

Lowe, R. J., J. L. Falter, M. D. Bandet, G. Pawlak, M. J. Atkinson, S. G. Monismith, and J. R. Koseff (2005), Spectral wave dissipation over a barrier reef, *J. Geophys. Res.*, *110*, C04001, doi:10.1029/2004JC002711.

Madsen, O., Y.-K. Poon, and H. Graber (1988), Spectral wave attenuation by bottom friction: Theory, in *Proceedings of the 21th International Conference on Coastal Engineering*, pp. 492–504, ASCE Press, Reston, Va.

Malhadas, M. S., P. C. Leitão, A. Silva, and R. Neves (2009), Effect of coastal waves on sea level in Óbidos Lagoon, Portugal, *Cont. Shelf Res.*, *29*(9), 1240–1250, doi:10.1016/j.csr.2009.02.007.

Marchesiello, P., J. C. Mcwilliams, and A. Shchepetkin (2001), Open boundary conditions for long-term integration of regional oceanic models, *Ocean Modell.*, *3*, 1–20.

Martins, F., P. C. Leitão, A. Silva, and R. J. J. Neves (2001), 3D modelling in the Sado estuary using a new generic vertical discretization approach, *Oceanol. Acta*, *24*(1), 51–62.

Mc Williams, J. C., J. M. Restrepo, and E. M. Lane (2004), An asymptotic theory for the interaction of waves and currents in coastal waters, *J. Fluid Mech.*, *511*, 135–178.

Mellor, G. (2003), The three-dimensional current and surface wave equations, *J. Phys. Oceanogr.*, *33*, 1978–1989.

Michaud, H., P. Marsaleix, Y. Leredde, C. Estournel, F. Bourrin, F. Lyard, C. Mayet, and F. Ardhuin (2012), Three-dimensional modelling of wave-induced current from the surf zone to the inner shelf, *Ocean Sci.*, *8*, 657–681, doi:10.5194/os-8–657-2012.

Miche, A. (1944), Mouvements ondulatoires de la mer en profondeur croissante ou décroissante. forme limite de la houle lors de son déferlement. application aux digues maritimes. exposé préliminaire, *Ann. Ponts Chaussées, Tome*, *114*, 25–42.

Montero, P. (1999), Estudio de la hidrodinamica de la ria de vigo mediante un modelo de volumenes finitos, PhD thesis, Univ. de Santiago de Compostela, Spain.

Nunes, V., and G. Pawlak (2008), Observations of bed roughness of a coral reef, *J. Coastal Res.*, *24*(2A), 39–50.

Pereira, P., H. De Pablo, C. Vale, V. Franco, and M. Nogueira (2009), Spatial and seasonal variation of water quality in an impacted coastal lagoon (Obidos Lagoon, Portugal), *Environ. Monit. Assess.*, *153*(1–4), 281–292.

Reeves, R. L., S. B. Grant, R. D. Mrse, C. M. Copil Oancea, B. F. Sanders, and A. B. Boehm (2004), Scaling and management of fecal indicator bacteria in runoff from a coastal urban watershed in southern California, *Environ. Sci. Technol.*, *38*(9), 2637–2648.

Reniers, A. J. H. M., J. H. MacMahan, E. B. Thornton, T. P. Stanton, M. Henriquez, J. W. Brown, J. A. Brown, and E. Gallagher (2009), Surf zone surface retention on a rip-channeled beach, *J. Geophys. Res.*, *114*, C10010, doi:10.1029/2008JC005153.

Riflet, G., G. Reffray, R. Fernandes, P. Chambel, J. Nogueira, and R. Neves (2010), Downscaling a large-scale ocean-basin model: An intercomparison exercise in the Bay of Biscay, in *Proceeding of the Vth European Conference on Computational Fluid Dynamics ECCOMAS CFD 2010*. APMTAC/IDMEC, Lisbon, Portugal.

Rodi, W. (1980), *Turbulence Models and Their Application in Hydraulics: A State of the Art Review*, 115 pp., Int. Assoc. for Hydraul. Res., Madrid, Spain.

Soloviev, A., and R. Lukas (2003), Observation of wave-enhanced turbulence in the near-surface layer of the ocean during TOGA COARE, *Deep Sea Res., Part I*, *50*(3), 371–395.

Soulsby, R. L., M. Stive, H. de Vriend, J. Fredsoe, L. Hamm, C. Teisson, and J. Winterwerp (1995), Bed shear stresses due to combined waves and currents, in *Advances in Coastal Morphodynamics*, pp. 4–20–4–23, Delft Hydraulics, Delft, Netherlands.

Spydell, M., F. Feddersen, R. T. Guza, and W. E. Schmidt (2007), Observing surf-zone dispersion with drifters, *J. Phys. Oceanogr.*, *37*(12), 2920.

Spydell, M., F. Feddersen, and R. T. Guza (2009), Observations of drifter dispersion in the surfzone: The effect of sheared alongshore currents, *J. Geophys. Res.*, *114*, C07028, doi:10.1029/2009JC005328.

Stokes, G. G. (1847), On the theory of oscillatory waves, *Trans. Cambridge Philos. Soc.*, *8*(441), 441–455.

Svendsen, I. A., and U. Putrevu (1994), Nearshore mixing and dispersion, *Proc. R. Soc. London, Ser. A*, *445*(1925), 561–576.

Terray, E. A., M. A. Donelan, Y. C. Agrawal, W. M. Drennan, K. K. Kahma, A. J. Williams, P. A. Hwang, and S. A. Kitaigorodskii (1996), Estimates of kinetic energy dissipation under breaking waves, *J. Phys. Oceanogr.*, *26*(5), 792–807.

Terray, E. A., W. M. Drennan, and M. A. Donelan (2000), The vertical structure of shear and dissipation in the ocean surface layer, in *Proceedings of the Symposium on Air-Sea Interaction, Sydney*, pp. 239–245, Univ. of N. S. W., Sydney, N. S. W.

Thornton, E. B., and R. T. Guza (1986), Surf zone longshore currents and random waves: Field data and models, *J. Phys. Oceanogr.*, *16*, 1165–1178.

Tolman, H. L. (2002), Validation of WAVEWATCH-III version 1.15, Washington, USA, *Tech. Rep. 213*, National Oceanic and Atmospheric Administration (NOAA)/National Weather Service (NWS)/National Centers for Environmental Prediction (NCEP)/Marine Modeling and Analysis Branch (MMAB), Washington, D. C.

Tolman, H. L. (2008), A mosaic approach to wind wave modeling, *Ocean Modell.*, *25*(1–2), 35–47.

Tolman, H. L. (2009), User manual and system documentation of WAVEWATCH III, *Analysis*, *166*(276), 220.

Uchiyama, Y., J. C. McWilliams, and J. M. Restrepo (2009), Wave-current interaction in nearshore shear instability analyzed with a vortex force formalism, *J. Geophys. Res.*, *114*, C06021, doi:10.1029/2008JC005135.

Uchiyama, Y., J. C. McWilliams, and A. F. Shchepetkin (2010), Wave-current interaction in an oceanic circulation model with a vortex-force formalism: Application to the surf zone, *Ocean Modell.*, *34*(1–2), 16–35, doi:10.1016/j.ocemod.2010.04.002.

UNESCO (1981), Tenth Report on the joint panel on oceanographic tables and standards, *Tech. Pap. Mar. Sci. 36*, 24 pp., UNESCO (United Nations Educational, Scientific and Cultural Organization), Paris, France.

Weir, B., Y. Uchiyama, E. M. Lane, J. M. Restrepo, and J. C. McWilliams (2011), A vortex force analysis of the interaction of rip currents and surface gravity waves, *J. Geophys. Res.*, *116*, C05001, doi:10.1029/2010JC006232.